Chapter 6: Results

Summary

Significant results regarding the kinetics of organometallic synthesis and the performance of CdSe quantum dots grown in different solvents are shown in Table 3. The activation energy, Q, for organometallic synthesis depended on the choice of solvent as follows: trioctylphosphine oxide (TOPO, $Q = 0.92 \pm 0.26$ eV), dodecylamine (DA, $Q = 1.05 \pm 0.1$ eV), and stearic acid (SA, $Q = 590 \pm 5$ eV). Compared to growth in TOPO or DA, CdSe nanocrystals grew more rapidly in SA, and produced narrow photoluminescence (PL) emission peaks at longer wavelengths, before the onset of Ostwald ripening.

In all synthesis solvents, the maximum photoluminescence quantum yield (PLQY) was near $26 \pm 3\%$, and the PLQY varied significantly with growth conditions. During fixed temperature runs, quantum dots exhibited locally higher PLQY at shorter emission wavelengths and shorter reaction times before the narrowest emission peaks were produced. Increasing the synthesis temperature generally decreased the reaction time needed to achieve a given wavelength. Generally, for growth in a given solvent, the evolution of PLQY and emission peak width correlated more consistently with the emission wavelength than with the synthesis temperature. Some exceptional properties occurred at ideal temperatures that depended on the solvent.

Higher selenium levels lead to the formation of more initial nuclei, which in turn increased the rate at which Cd precursors were depleted. Even so, the evolution of

quantum dot radius, determined by the first absorbance peak position, was virtually unaffected by the initial Cd:Se precursor ratio. Growth of CdSe quantum dots during the early stages of organometallic synthesis was reasonably well described by an analytical model of the diffusion and depletion of reactants.

Table 3. Summary of CdSe quantum dot performance and synthesis kinetics.

Solvent	TOPO	Stearic acid	Dodecylamine
Mol. Weight (g/mole)	386.65	284.47	185.35
Q (eV)	0.92 ± 0.26	0.6 ± 0.1	1.05 ± 0.1
Width (%)	2.0 – 4.8	2.0 –3.7	2.2 – 2.8
PLQY (% of R-6G)	0 – 29	0 – 23	0 – 28
Narrowest λ_{PL} (nm)	555 ± 5	590 ± 5	570 ± 5
Brightest λ_{PL} (nm)	520 ± 20	560 ± 10	512 – 528
Optimum Temp. (^{o}C)	300	255	195

Transition Energies

Excitation spectra were acquired by fixing the detector wavelength at the peak photoluminescence emission wavelength, with narrow 2.5 nm slits, while varying the excitation wavelength. Excitation spectra were acquired for selected samples of CdSe quantum dots, and typical results are shown in Figure 6-1. The sharp peak at 2.2 eV, which results when the excitation exactly matches the detector wavelength, can be ignored. The lowest optical transition occurs at 2.23 eV, and the next optical transition

occurs at 2.7 eV, so that the size-dependent energy shaft away from E_g (1.7 eV) is 0.53 eV and 1.0 eV, respectively. The ratio of the second transition energy divided by the first transition energy is 1.9 ± 0.1, which agrees with the 2.05 predicted by the effective mass approximation theory.

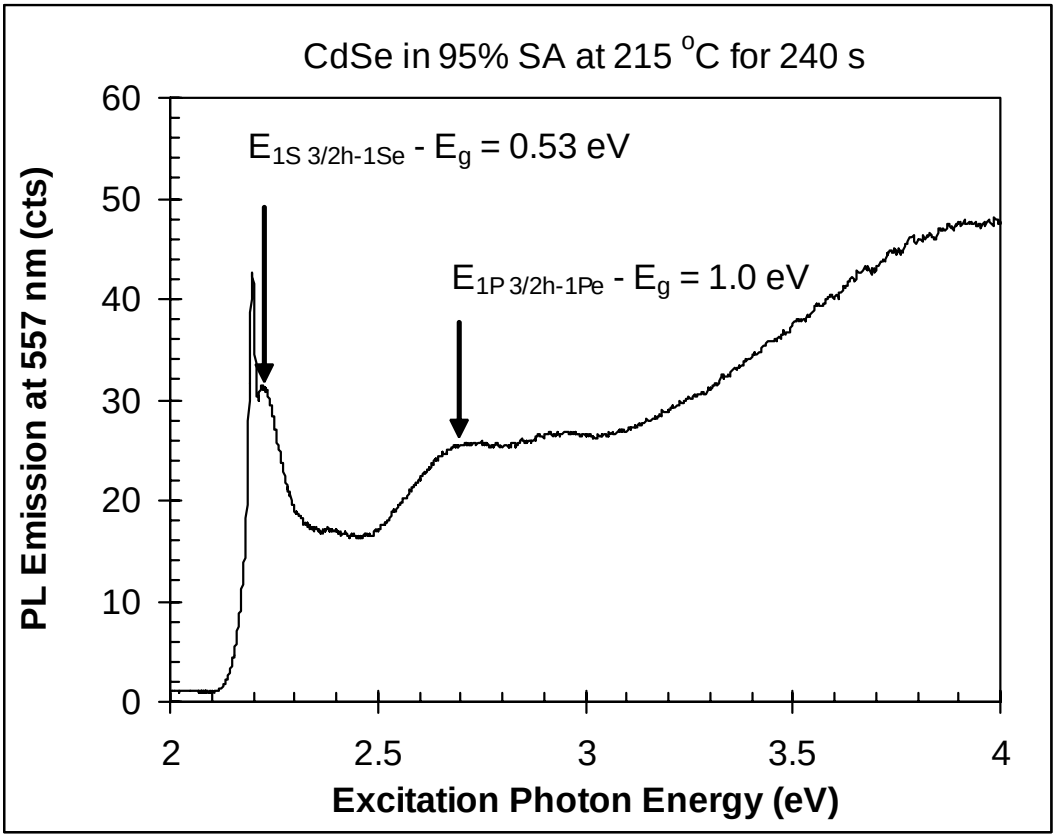

Figure 6-1. Typical excitation spectrum of CdSe quantum dot solution. The ratio the size-dependent energy shifts for the two designated transitions is 1.9 ± 0.1, in agreement with 2.05 predicted by the effective mass approximation theory.[26]

Obtaining PLQY Estimates from PL Spectra

Ideally, the integrated photoluminescence, Ψ_{QD}, of each quantum dot sample would be compared to that of a reference sample with the same absorbance at the excitation wavelength. Rather than prepare a separate reference solution for every

quantum dot sample, a representative series of dilute rhodamine 6G solutions with known concentrations was prepared, with peak absorbance values at 500 nm, A_{R6G}, ranging from 0.02 to 0.07 cm^{-1}. Figure 6-2 shows that the net photoluminescence, $I_{R6G,}$ (integrated counts from 515 nm to 720 nm) was proportional to A_{R6G}. That is, $\Psi_{R6G} = C * A_{R6G}$, where $C = 1.0406 \times 10^7$ (counts-cm). Therefore, in calculations of PLQY, this linear equation was used to estimate the photoluminescence of desired rhodamine 6G reference solutions that would match each quantum dot sample.

To illustrate this process, typical absorbance spectra for a rhodamine 6G solution and a CdSe quantum dot solution are overlaid in Figure 6-3. The shoulder in rhodamine 6G absorbance at 500 nm provided a convenient excitation wavelength that is shorter than the primary absorbance peak at 533.5 nm.

In order to compare the relative emission intensity of CdSe quantum dots to rhodamine 6G standards that have absorbed the same amount of light, each quantum dot solution was diluted so that the value of its absorbance at 500 nm, minus the absorbance background at about 650 nm, was close to 0.05, as shown in Figure 6-3. The results of a typical PL test are shown in Figure 6-4. The rhodamine 6G solution has an emission peak at 555 nm that is significantly higher than the quantum dot emission peak. The standard measurements of PLQY could only be performed on QD solutions emitting within 5 nm of 555 nm, using Equation (6-1), where Ψ is the area under the PL curve. To estimate PLQY for samples emitting at other wavelengths, regular PL spectra were also acquired, with excitation at 370 nm. Within sets of samples synthesized at the same reaction temperature, the emission amplitude was always compared to that of samples emitting near 555 nm, using Equation (6-2). For improved accuracy of these extended

PLQY estimates, a multiplying correction factor could also be inserted to account for variations in the absorbance of each sample at 370 nm, but this was not included in the results shown.

$$PLQY_{relative} = 100\,\Psi_{QD555} / \Psi_{R6G} \qquad \text{for PL emission near 555 nm} \qquad (6\text{-}1)$$

$$PLQY_{aprox} = PLQY_{relative}\,\Psi_{QD\lambda} / \Psi_{QD555} \qquad \text{for PL emission away from 555 nm} \qquad (6\text{-}2)$$

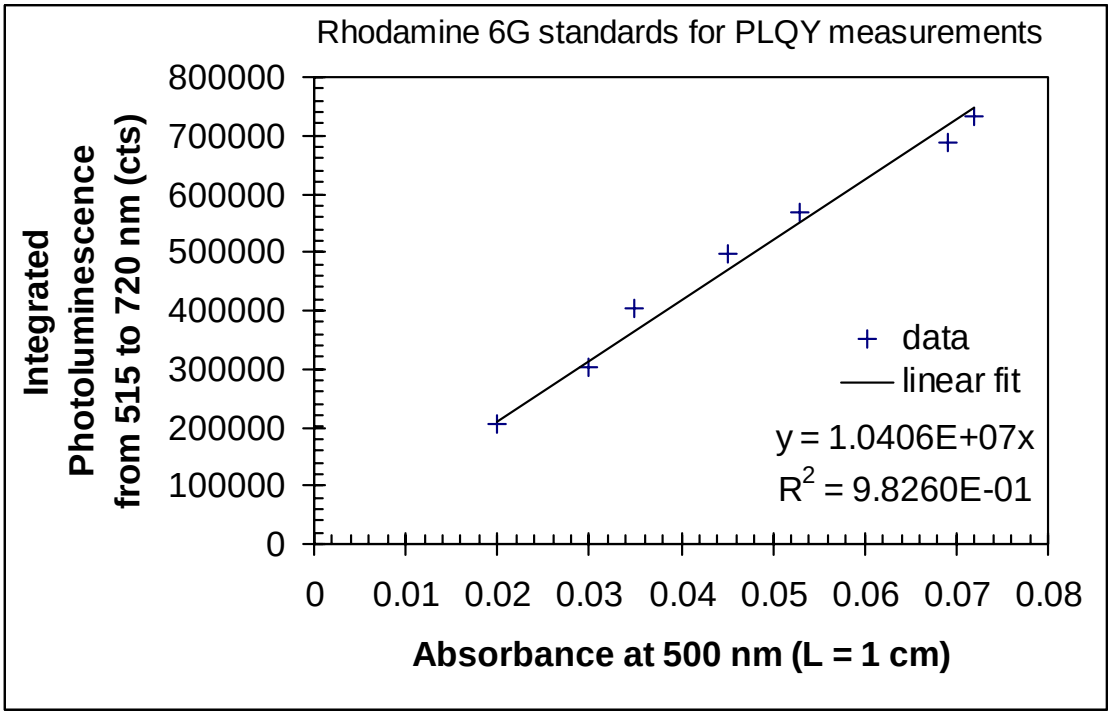

Figure 6-2. Integrated photoluminescence of rhodamine 6G standards. For solutions diluted so that absorbance was less than 0.07 at 500 nm, photoluminescence was proportional to absorbance. The linear fit was used to estimate the integrated PL counts of standard solutions with absorbance at 500 nm exactly matching that of QD samples.

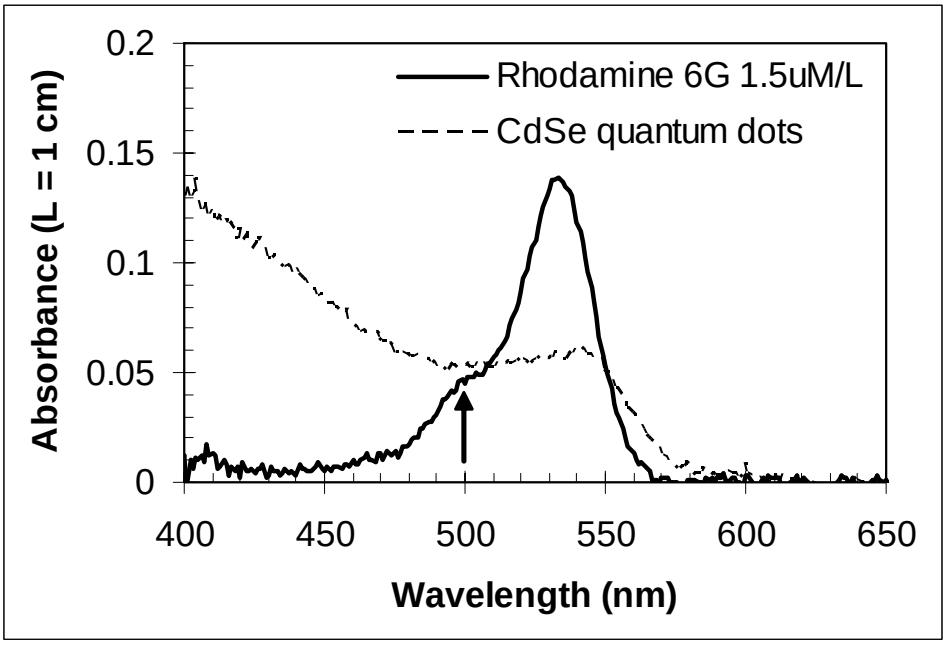

Figure 6-3. Absorbance spectra of rhodamine 6G and CdSe quantum dot solutions. These CdSe quantum dots were grown in SA for 6 minutes at 205 ^{o}C. Both solutions were diluted in a 1:8 volume mixture of methanol and toluene to achieve an absorbance of about 0.05 at 500 nm, marked by the arrow.

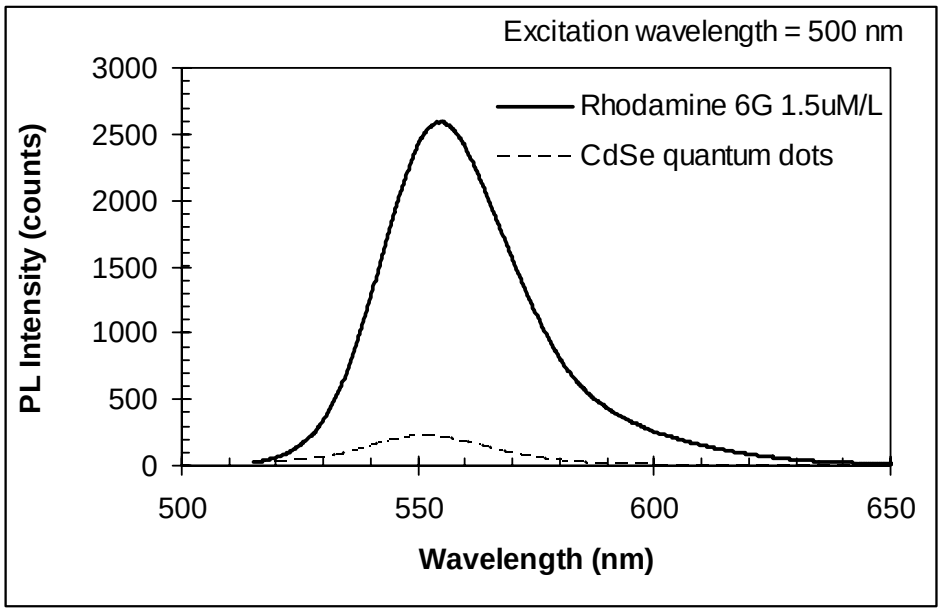

Figure 6-4. Comparing CdSe quantum dots to rhodamine 6G for PLQY estimate. The integrated area under the quantum dot PL curve was 7.7% of the area under the PL curve of a rhodamine 6G solution with the absorbance at the excitation wavelength matched to the quantum dot sample, so the photoluminescence quantum yield of these quantum dots was 7.7% of rhodamine 6G's PLQY, which is 95.5%.

Evolution of PL Spectra with Reaction Time

Normal PL spectra, with excitation at 370 nm, required subtraction of a scaled background curve, as shown in Figure 6-5. The background curve came from PL emission from samples containing only precursors but no quantum dots. After background subtraction, samples exhibited Gaussian distributions of PL emission versus photon energy. The characteristic amplitude, mean, and standard deviation of these emission distributions were extracted using KaleidaGraph curve-fitting software.

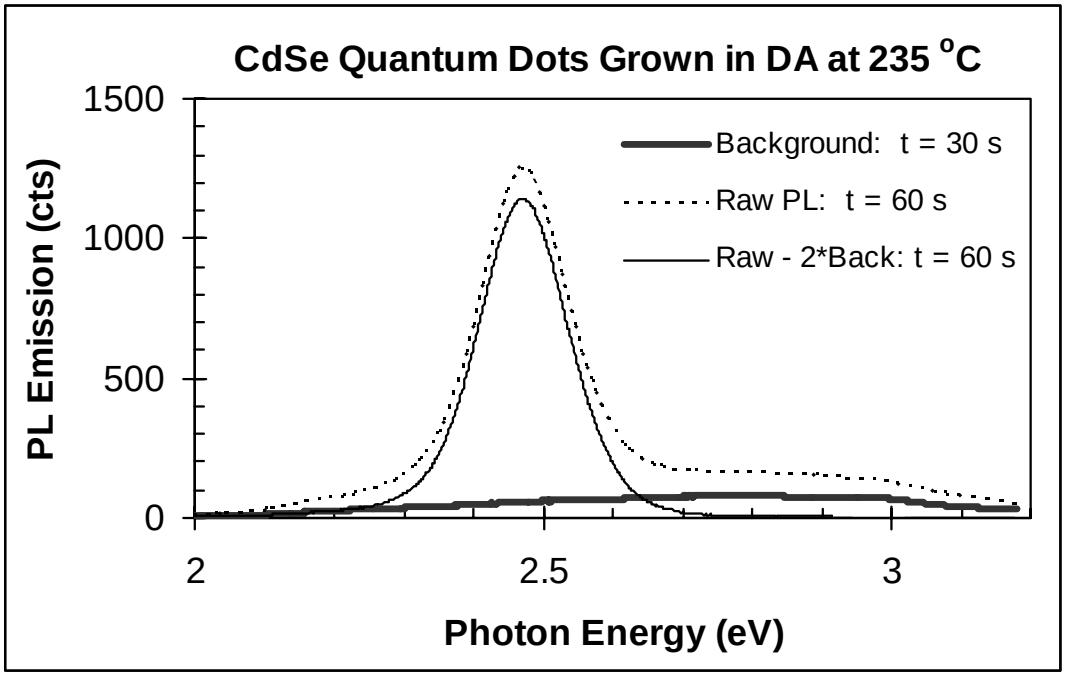

Figure 6-5. Processing PL spectra by applying a background subtraction.

The evolution of PL spectra with reaction time at 235 °C for growth in dodecylamine (DA), trioctylphosphine oxide (TOPO), and stearic acid (SA) are shown in Figures 6-6, 6-7 and 6-8, respectively. Typically the PL intensity grows to a maximum at some intermediate reaction time and then steadily decreases for longer reaction times.

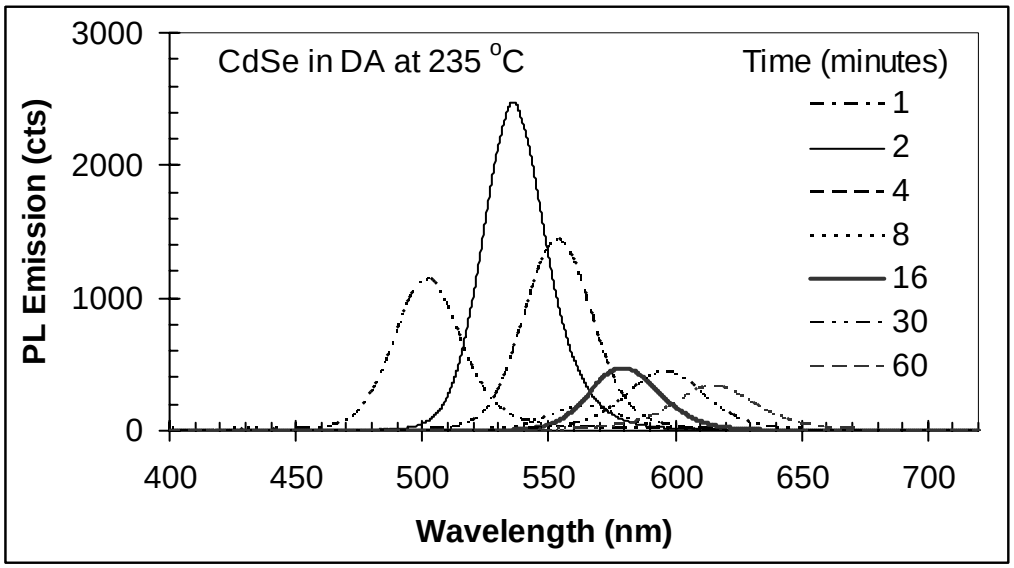

Figure 6-6. PL spectra for CdSe quantum dots grown in dodecylamine (DA) at 235 °C.

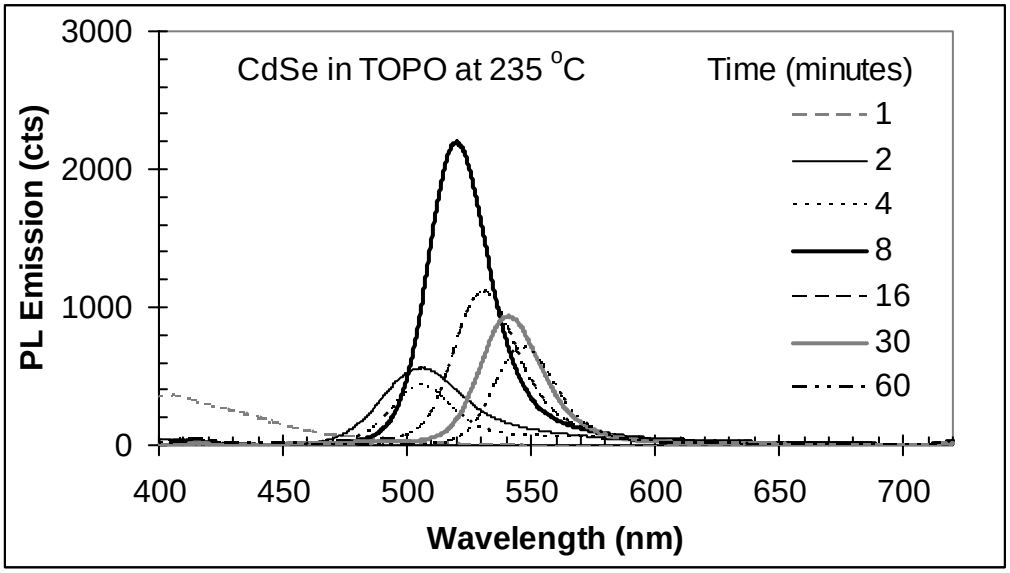

Figure 6-7. PL spectra for CdSe quantum dots grown in TOPO at 235 °C.

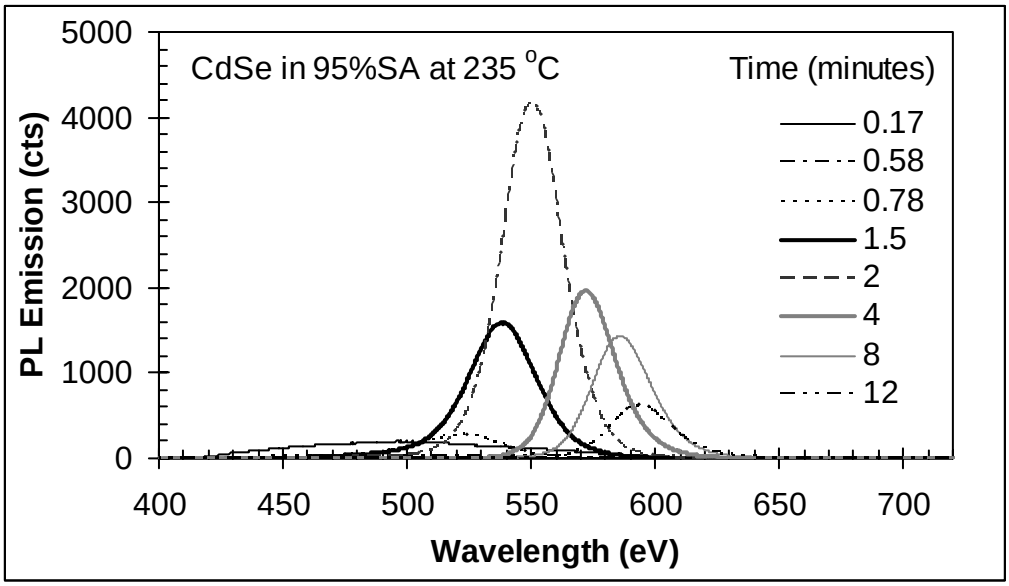

Figure 6-8. PL spectra for CdSe quantum dots grown in stearic acid (SA) at 235 °C.

Of course the peak emission wavelength moves towards longer wavelengths with longer reaction times. The brightest PL emission is usually observed when the emission wavelength is somewhere between 500 nm and 550 nm. For growth at 235 °C, the brightest emission occurs for quantum dots grown in stearic acid after 2 minutes, and the next brightest in DA after 2 minutes; to produce that same brightness in TOPO, four times longer synthesis time (8 minutes) is needed.

The red-shifting of the peak PL wavelength with progressively longer reaction times is clearly shown in Figure 6-9. For all samples, emission wavelength increased rapidly with reaction time early during organometallic synthesis, but then stabilized towards some critical wavelength, λ_c, for longer synthesis times. This critical wavelength became progressively longer as the reaction solvent was changed from TOPO to DA to SA. Changing solvents in the same order also decreased the time required to achieve emission at 550 nm, for example. Growth rates and emission wavelengths from CdSe quantum dots synthesized in dodecylamine were generally between those observed after

synthesis in TOPO and stearic acid under the same experimental conditions of reaction time and temperature.

Focusing and defocusing of emission peak width occurred with reaction time, as seen in Figure 6-10. The minimum width may occur early or late in reaction depending on the choice of solvent. The PLQY was optimized somewhere in the middle of synthesis (Figure 6-11), following the trends in emission amplitude discussed earlier.

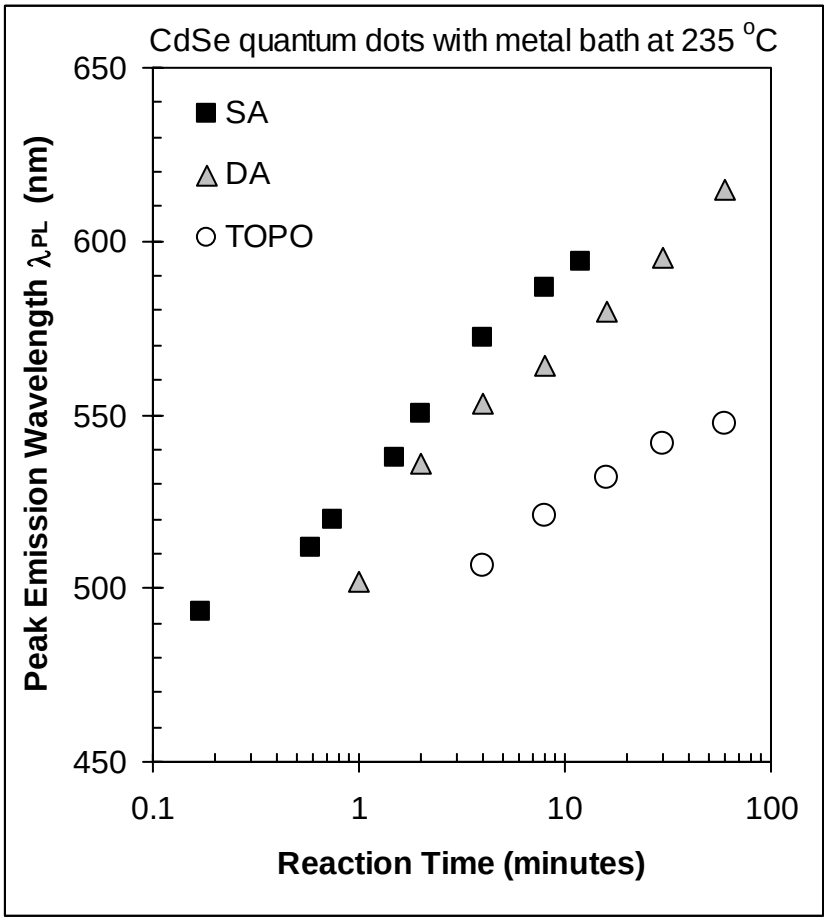

Figure 6-9. Evolution of emission wavelength with reaction time at 235 °C for different solvents.

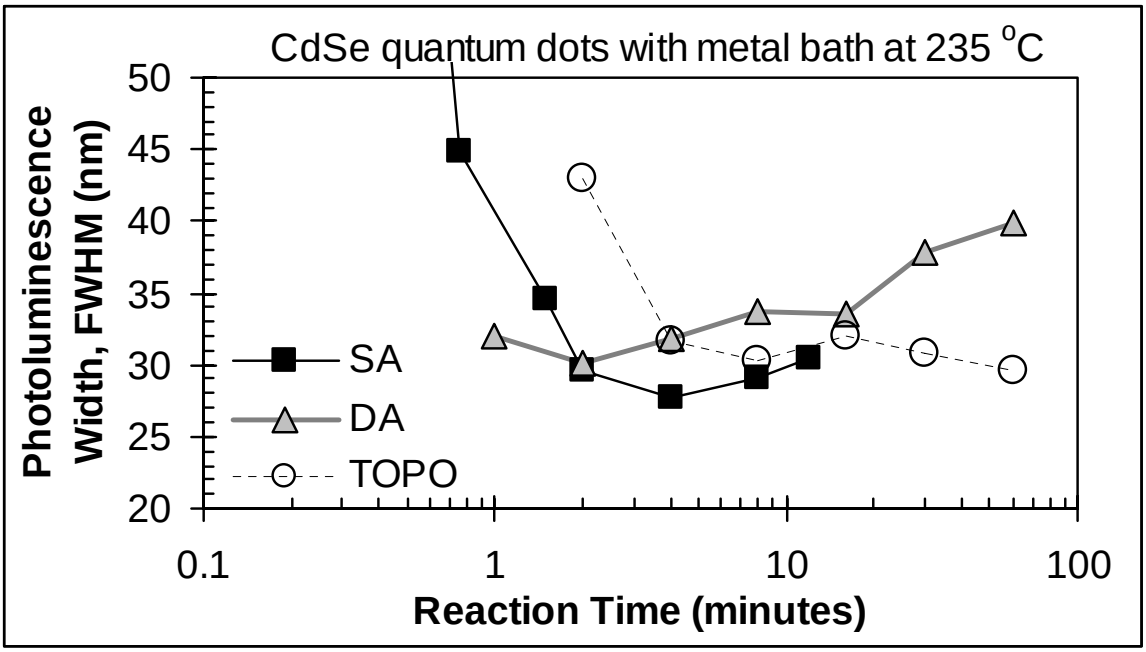

Figure 6-10. Relative PL emission width versus time at 235 °C for all three solvents.

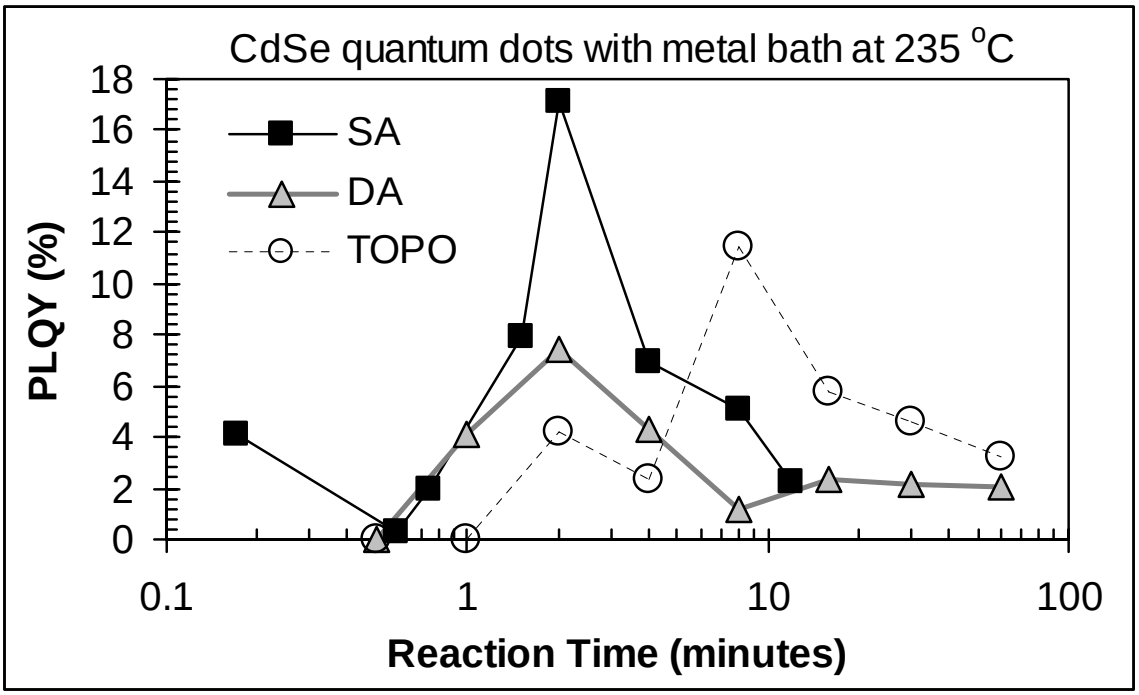

Figure 6-11. PLQY versus synthesis time at 235 °C for all three solvents.

Maps of Performance Versus Synthesis Conditions

Color topographical maps were produced to show how the PL emission peak wavelength was tailored by adjusting the synthesis temperature and the reaction time for synthesis in DA, TOPO, and SA (Figures 6-12, 6-13, and 6-14, respectively). Colors from blue to orange were achieved, covering most of the visible spectrum. Longer wavelengths were produced by increasing the synthesis time or the synthesis temperature. Increasing the synthesis temperature generally decreased the reaction time needed to achieve a given wavelength.

The horizontal axes show progressively doubling reaction times. For synthesis in DA (Figure 6-12) the similar horizontal spacing between isochromic lines indicates that progressively doubling reaction times were needed to produce about the same progressive red-shift of the PL peak wavelength across most of the visible spectrum. However when CdSe quantum dots are grown in TOPO (Figure 6-13), the wavelength leveled off at about 550 nm, regardless of the synthesis temperature; in other words, 550 nm is in the middle of a wide plateau. At temperatures above 325 °C, the slope of wavelength versus time (*i.e.* the red-shift rate) became steeper for wavelengths longer than 580 nm. This trend of a broad wavelength plateau followed by a steeper region at higher temperatures and longer reaction times is also seen in the topographical map of quantum dots grown in stearic acid (Figure 6-14).

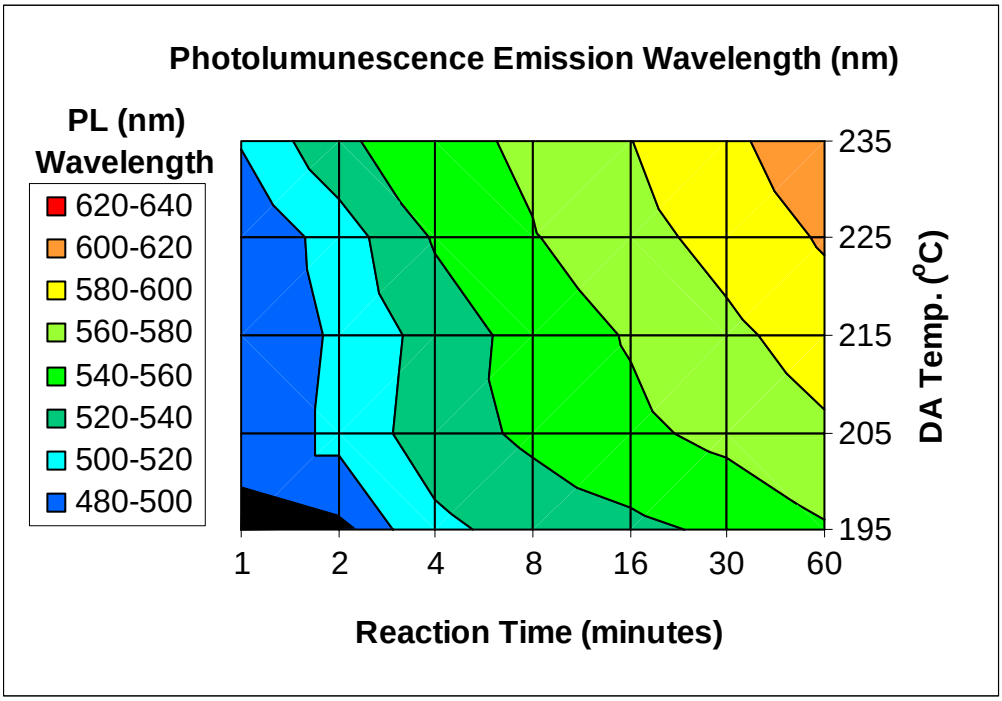

Figure 6-12. PL emission color versus of synthesis conditions in DA.

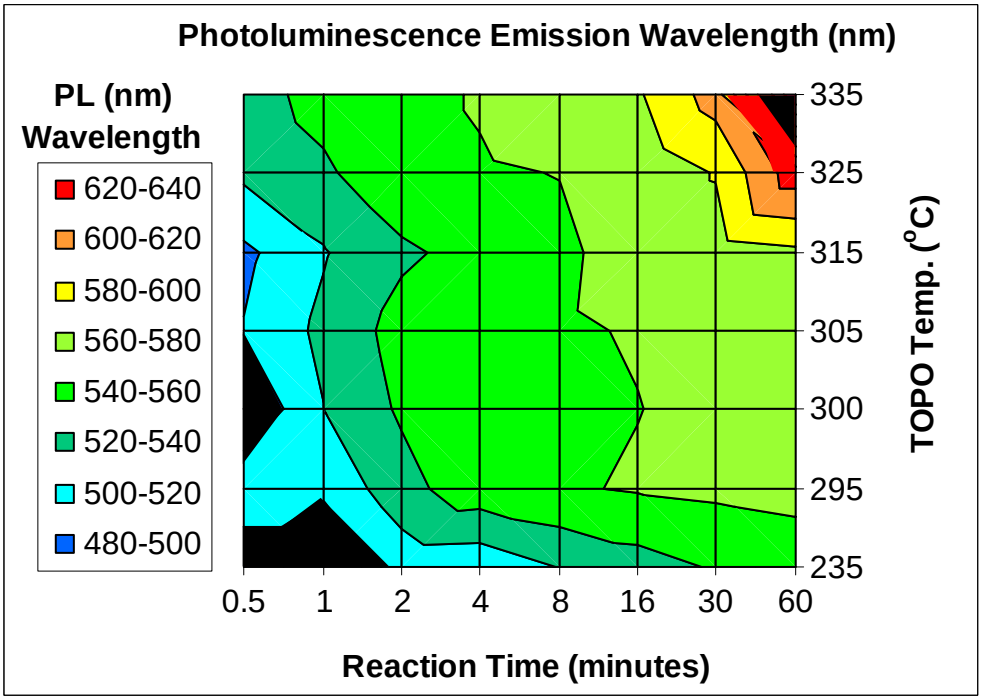

Figure 6-13. PL emission color versus of synthesis conditions in TOPO.

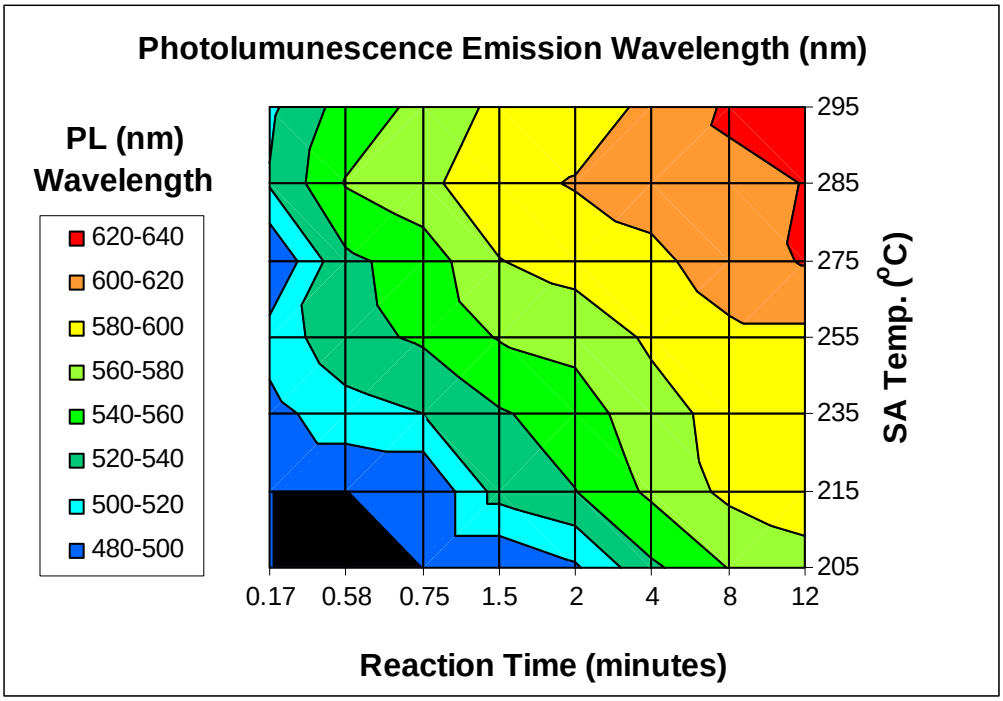

Figure 6-14. Color map for growth in SA.

For synthesis in DA, variation in emission width and PLQY with synthesis time and temperature are shown in Figures 6-15 and 6-16, respectively, with the same axes as in Figure 6-12. In Figure 6-15, narrower PL emission widths, σ/E_{PL}, are indicated by lighter colors. The sharpest PL peaks were observed for synthesis at 225 °C for 16 minutes, but a valley of narrow PL emission extended along the conditions which produced emission at 570 nm, indicated by a dashed line. Regardless of synthesis conditions, all observed emission peaks were fairly sharp for synthesis in DA, with σ/E_{PL} between the 2 and 3%.

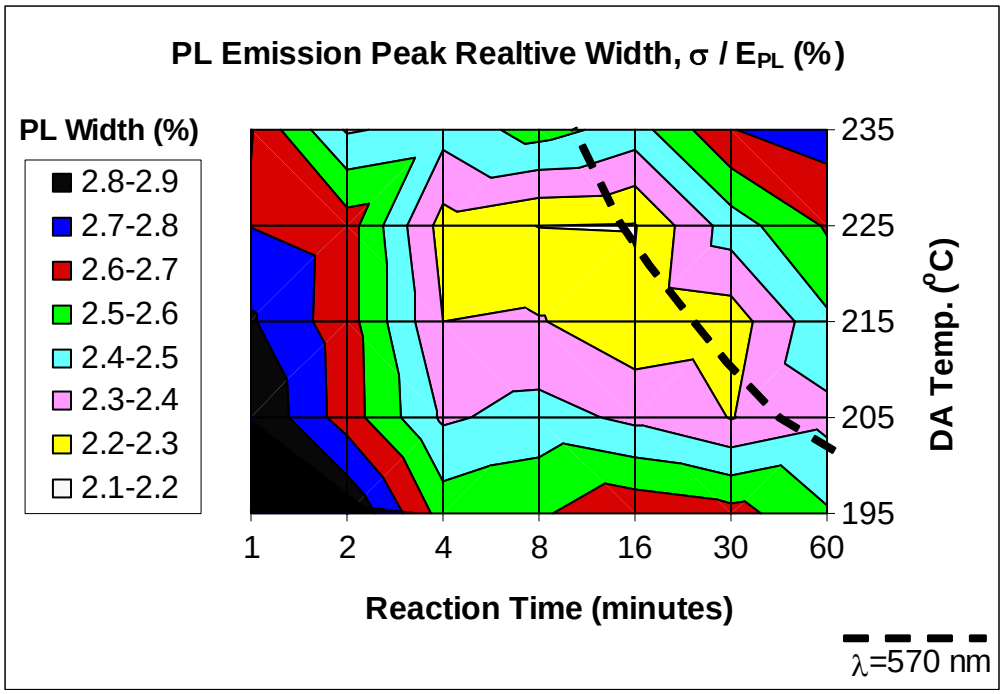

Figure 6-15. Map of PL emission width versus conditions for synthesis in DA.

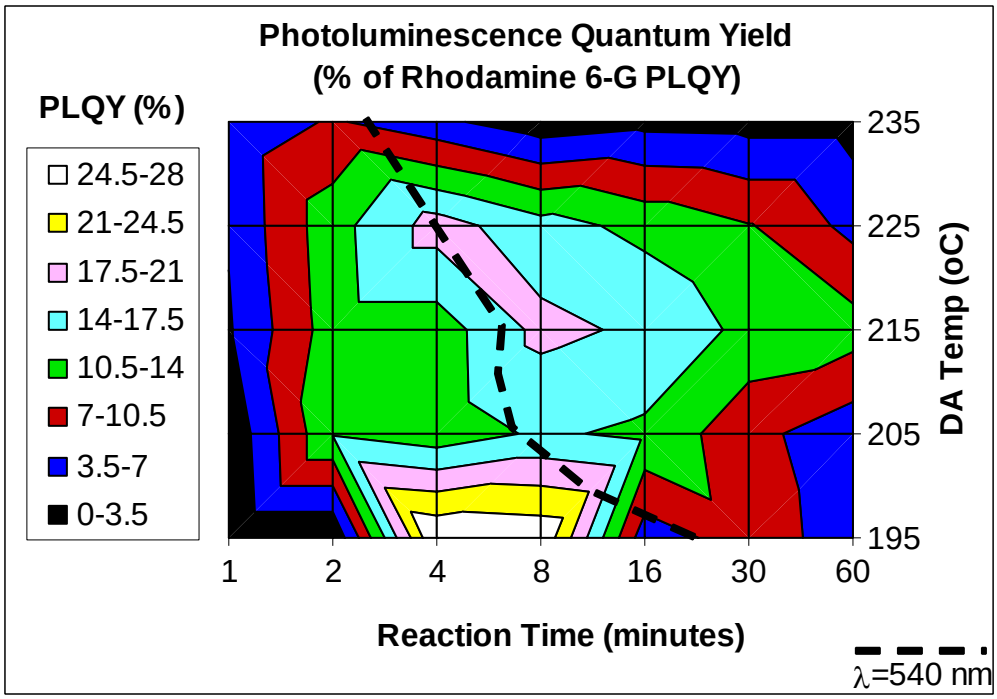

Figure 6-16. Map of PLQY versus conditions for synthesis in DA.

In Figure 6-16, brighter emission (*i.e.* higher PLQY) is indicated by lighter colors. In DA, growth at 195 °C from 4 to 8 minutes produced the highest PLQY (28%), but a secondary local maximum (~19%) for emission at 550 nm occurred for synthesis from 4 to 8 minutes between 215 and 225 °C. In most cases, using synthesis conditions that deviated from those of the secondary maximum dramatically reduced the PLQY.

For synthesis in TOPO, maps of emission width and PLQY are shown in Figures 6-17 and 6-18 respectively. All synthesis conditions produced narrow emission widths between 2 and 4%, but the valley of narrowest emission corresponded with conditions that produced 550 nm emission over a wide temperature range from 235 to 335 °C (Figure 6-17). There were also local minima at 295 °C and 315 °C. A map of PLQY versus time and temperature for synthesis in TOPO is shown in Figure 6-18. The conditions for highest PLQY often correlated with those that produced emission near 520 nm. But breaking this trend, synthesis at 300 °C produced higher PLQY at longer emission wavelengths. The maximum PLQY was 29% in TOPO, which was similar to the maximum PLQY of 28 % in DA.

For synthesis in stearic acid, the highest PLQY was 23%, which is slightly lower than in TOPO or DA. As usual, the reaction conditions which optimized emission width and PLQY are shown in lighter colors in Figures 6-19 and 6-20, respectively. The highest PLQY correlated with conditions that produced emission near 560 nm, while emission near 590 nm had the narrowest peaks.

Often the highest PLQYs occurred before the narrowest emission peaks were produced. In the same way, the highest PLQYs were associated with wavelengths that were shorter than those of the narrowest emission peaks.

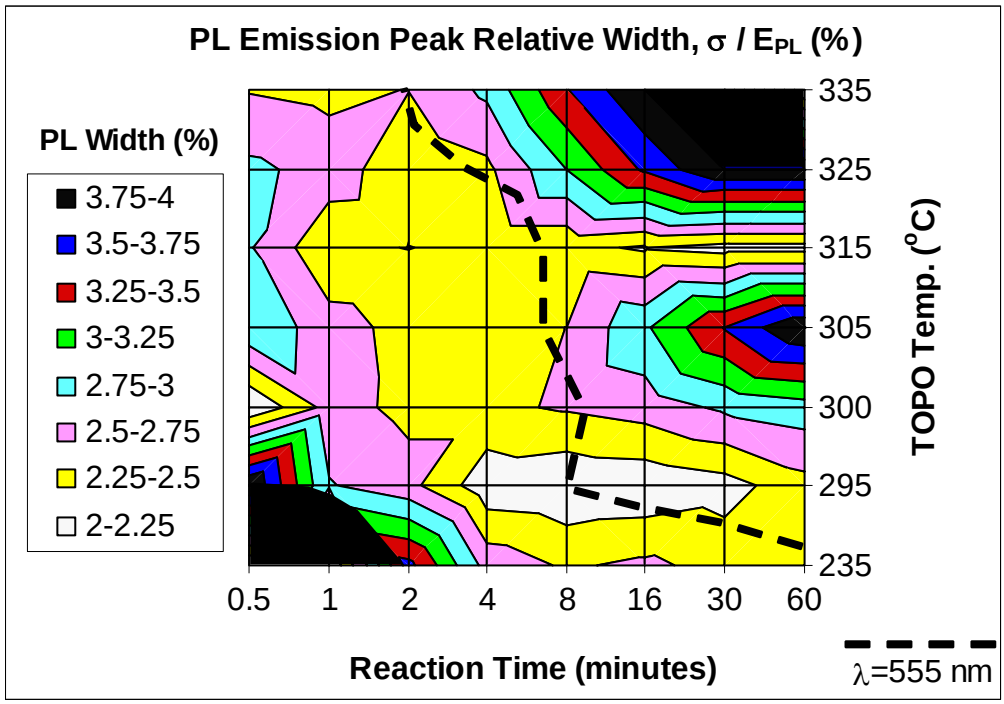

Figure 6-17. Map of PL emission width versus conditions for synthesis in TOPO.

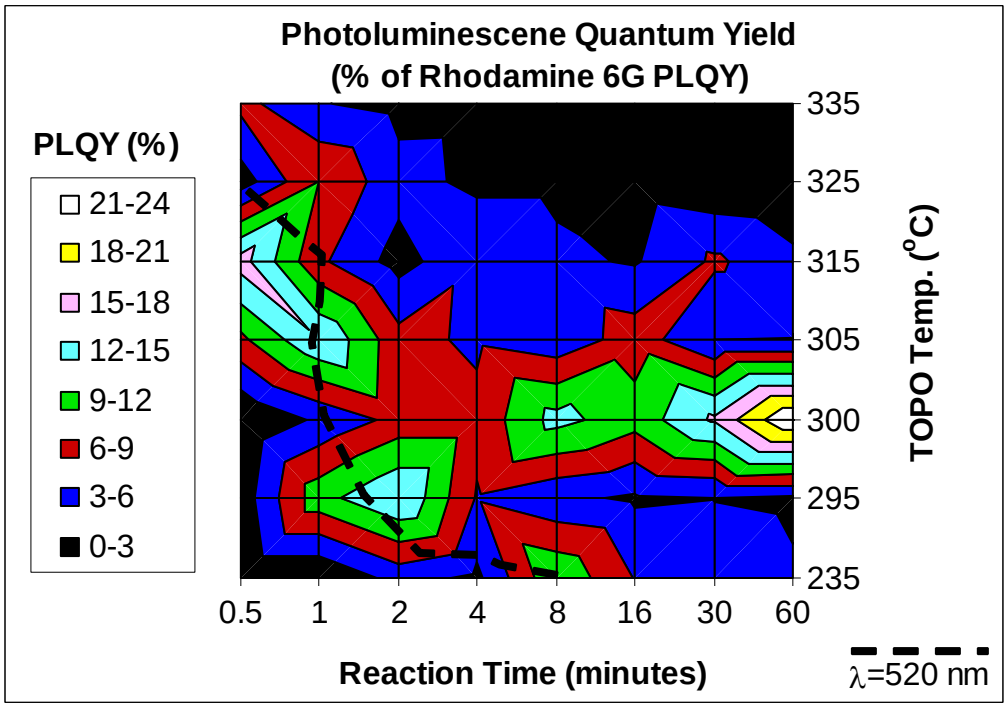

Figure 6-18. Map of PLQY versus conditions for synthesis in TOPO.

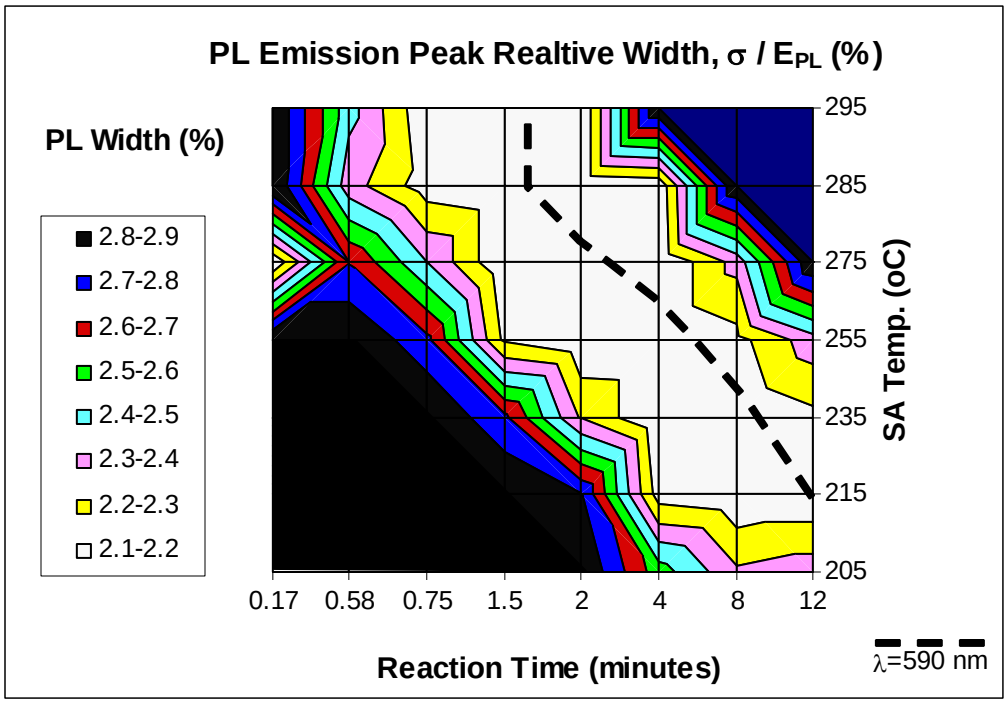

Figure 6-19. Map of PL emission width versus conditions for synthesis in SA.

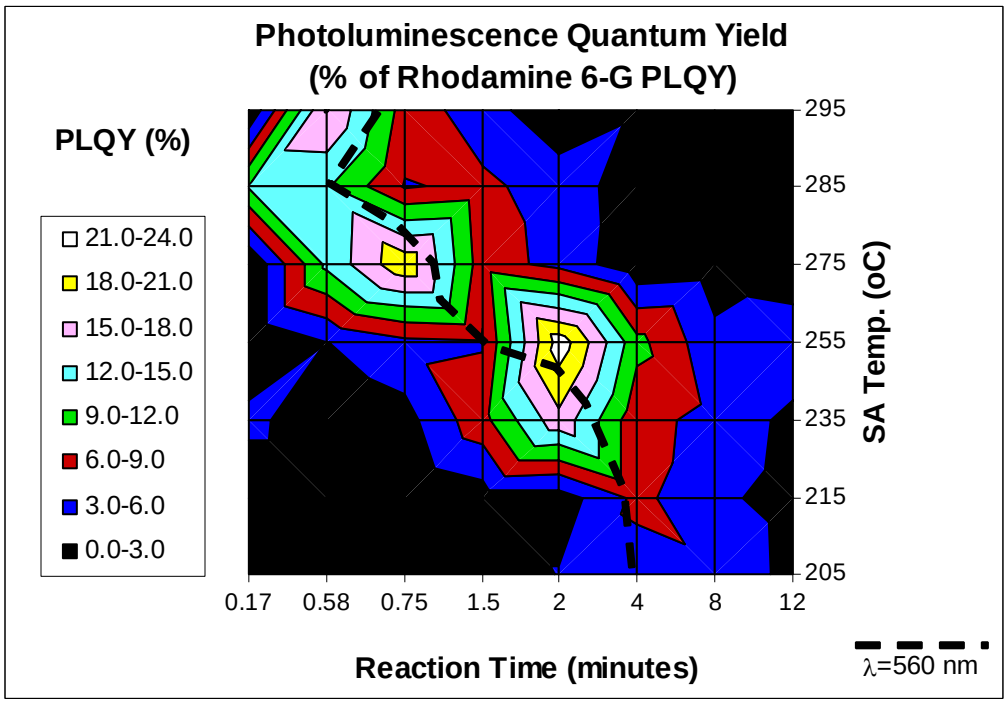

Figure 6-20. Map of PLQY versus conditions for synthesis in SA.

Estimating Synthesis Activation Energies from Growth Rates

Since PL emission wavelength can be used to probe nanocrystal radius, as discussed in Chapters 2 and 4, changes in emission wavelength are related to the nanocrystal growth rate. Figure 6-21 shows emission wavelength data from Figure 6-14 plotted in a more conventional way, for synthesis in stearic acid. In the present work, the redshift rate is defined as the change in emission wavelength divided by the change in reaction time between sequential samples. Each redshift rate is assigned to the average wavelength and the average time between sequential samples. In Figure 6-21, it is clear that the steeper slopes and therefore the highest redshift rates will occur at shorter reaction times and at higher synthesis temperature. Therefore higher redshift rates are seen in Figure 6-22 at shorter emission wavelengths and at higher synthesis temperatures.

By picking a common test wavelength (for example 540 nm, marked in Figure 6-22), the temperature dependence of red-shift rates can be analyzed. A typical Arrhenius plot of the natural log of the red-shift rate versus 1000/*T* is shown in Figure 6-23, using 540 nm as a test wavelength; a steeper slope indicates a higher activation energy in TOPO than in stearic acid.

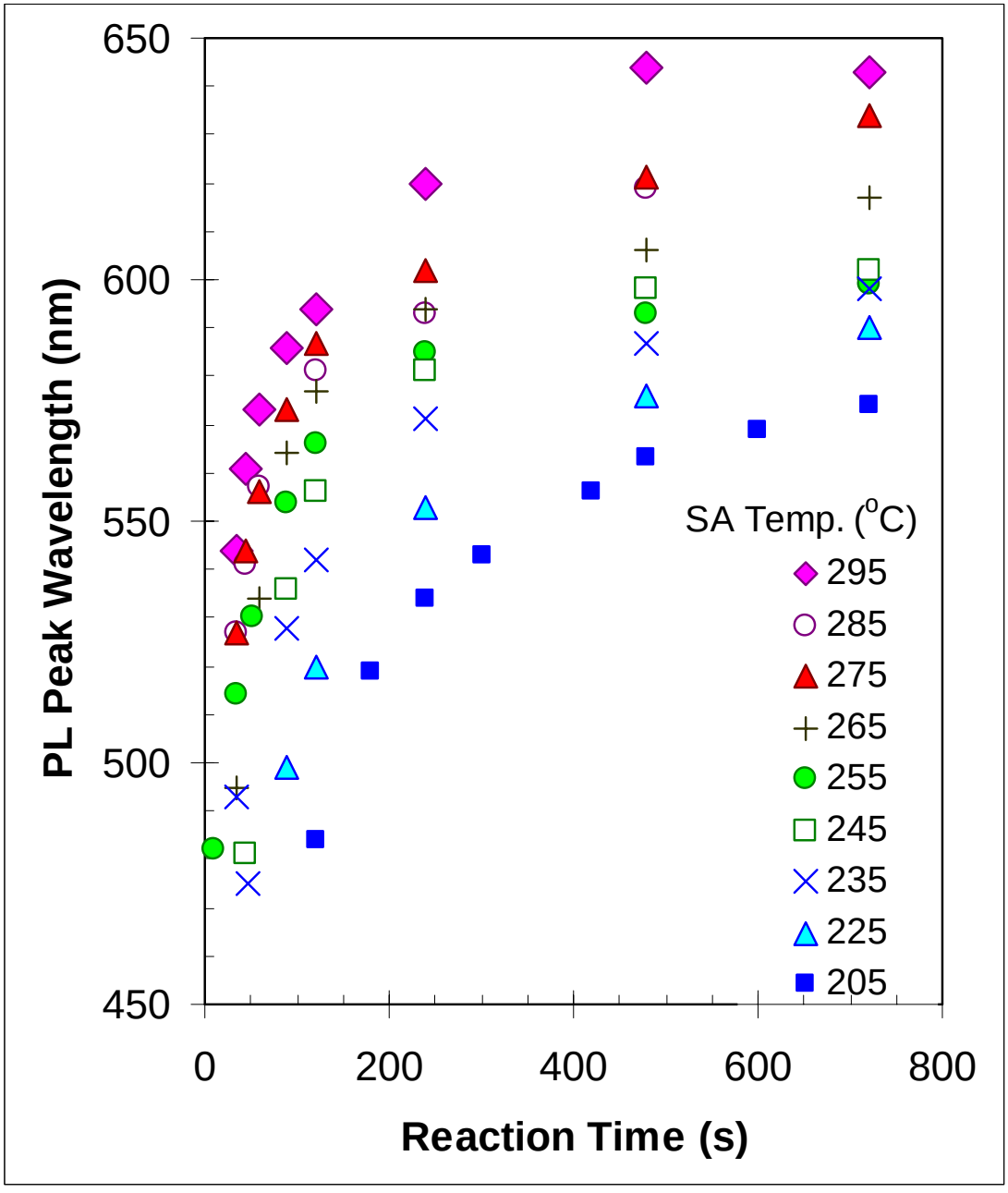

Figure 6-21. Evolution of λ_{PL} with reaction time in SA at different temperatures.

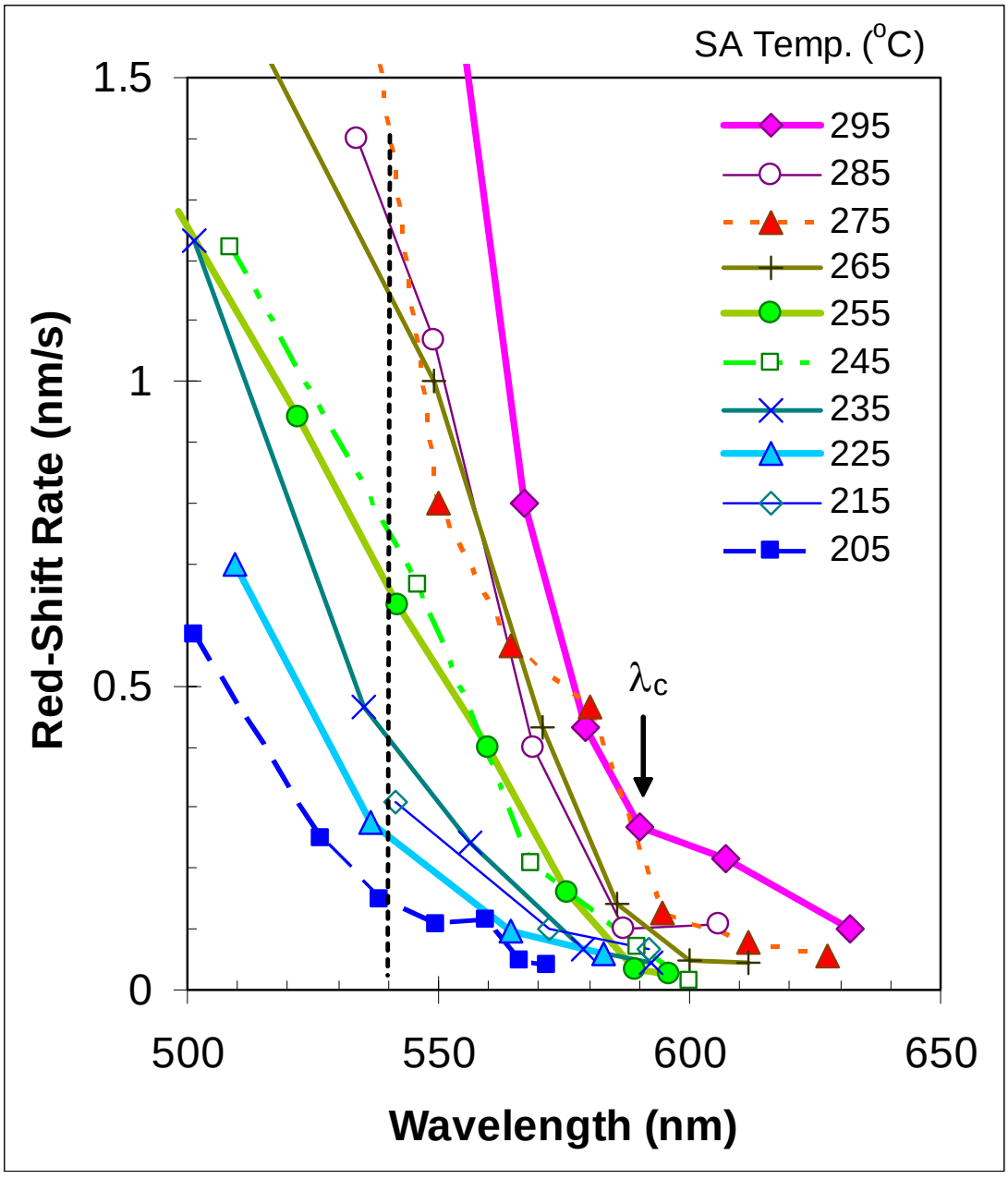

Figure 6-22. Redshift rates from the slope of λ_{PL} versus time for synthesis in SA. Regardless of temperature, all redshift rates reach a minimum for PL emission at λ_c = 590 nm for synthesis in stearic acid (SA). A test wavelength of 540 nm is marked, for Arrhenius analysis in Figure 6-23.

Experimentally, red-shift rates and PL peak widths both tend to decrease to a minimum as λ approaches a completion wavelength, λ_c, which is usually independent of synthesis temperature. For these QDs grown in SA, λ_c is 590 ± 5 nm, as seen in Figure 6-22. Coincidentally, in Figure 6-24, as the test wavelength was moved above 590 nm, the estimate of Q_{SA} for growth in SA sharply doubled to 1.25 ± 0.05 eV/molecule, suggesting a change in the dominant growth mechanism. These observations are consistent with the exhaustion of reactants at t_c, followed by the onset of Ostwald ripening. For CdSe QDs grown in TOPO, λ_c is 560 ± 5 nm. However Q_{TOPO} could not be accurately estimated from test wavelengths near 560 nm due to a limited range of chosen synthesis temperatures.

Systematic variation in Q with test wavelength is shown in Figure 6-24. Even so, red-shifts showed that the activation energy in TOPO (Q_{TOPO} = 0.95 ± 0.27 eV) was significantly higher than in stearic acid (Q_{SA} = 0.56 ± 0.12 eV).

Using the diffusion model derived in Chapter 4, the evolution of emission wavelength with reaction time was stimulated by adjusting the completion time to best fit PL data from reactions at different temperatures. Typical examples of such fits are shown in Figure 6-25, for synthesis in stearic acid. Typically the completion time corresponds with reaction time needed to achieve a PL wavelength near the knee of wavelength versus time. The model predicts that emission will stabilize at a critical wavelength, but experimental data shows that the emission wavelength can continue to increase beyond λ_c. Even after t_c, progressively higher red-shift rates occurred at progressively higher temperatures.

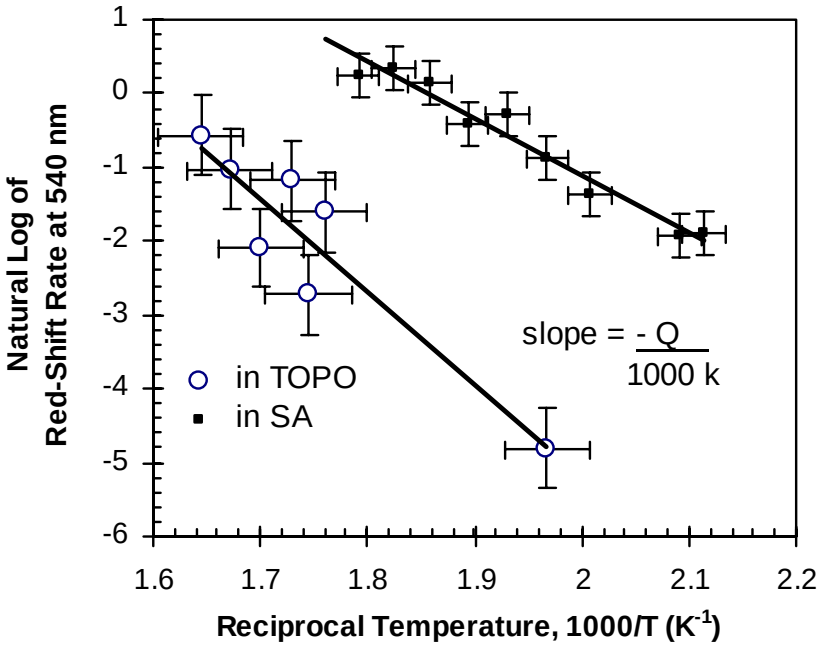

Figure 6-23. Arrhenius temperature dependence of red-shift rates at 540 nm. This figure was reprinted with permission from Dickerson et al., Appl. Phys. Lett., **86** 076518 (2005). Copyright 2005 American Institute of Physics.

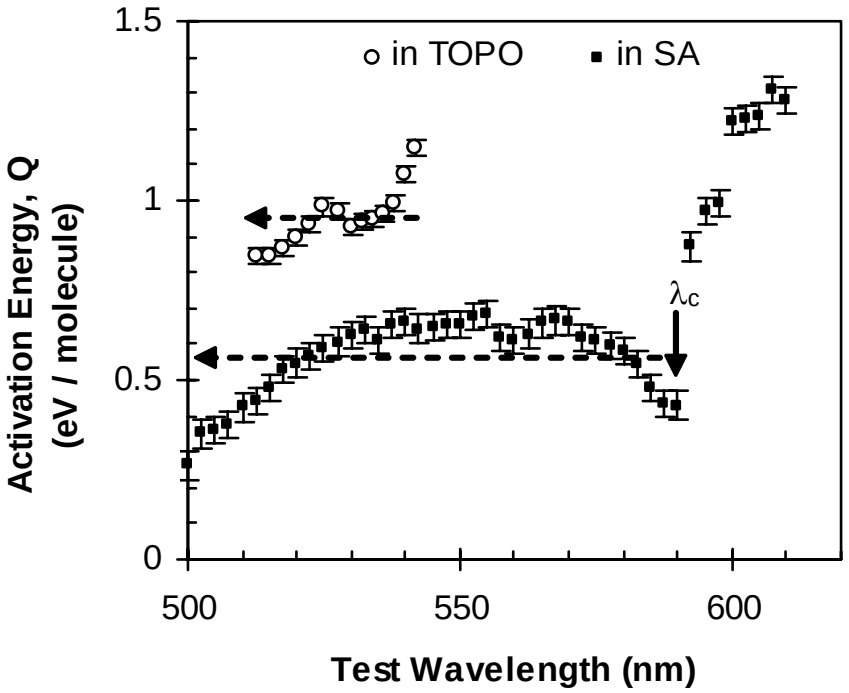

Figure 6-24. Activation energies from red-shift rates at different test wavelengths. This figure was reprinted with permission from Dickerson et al., Appl. Phys. Lett., **86** 076518 (2005). Copyright 2005 American Institute of Physics.

The quantity $1/t_c$ represents a reaction completion rate. So it is not surprising that an Arrhenius plot of the natural log of $1/t_c$ versus $1000/T$ yielded activation energies that agreed with those estimated from red-shift rates (Figure 6-26). In the diffusion model, the completion time and completion wavelength represent the reaction time and emission wavelength, respectively, at which all Cd precursor is exhausted. In Figure 6-27, the full width half max (FWHM) of emission from CdSe quantum dots grown in stearic acid is plotted versus the PL emission wavelength. Regardless of synthesis temperature, emission is narrowest at the completion wavelength.

Activation energies were also estimated from the temperature dependence of t_c. Experimental observations of λ vs. t were compared to modeled curves (Figure 6-25) to estimate t_c at each temperature. Then Q was calculated from the slope in a plot of $ln(1/t_c)$ vs. $1000/T$, shown in Figure 6-26. The activation energies calculated using t_c (Q_{SA} = 0.65 ± 0.07 eV/molecule and Q_{TOPO} = 0.89 ± 0.25 eV/molecule) agree with those estimated using red-shift rates, within experimental error. Estimating activation energies from the temperature dependence of completion rates, rather than from red-shift rates, reduces random and systematic errors by analyzing overall trends rather than local trends in PL evolution.

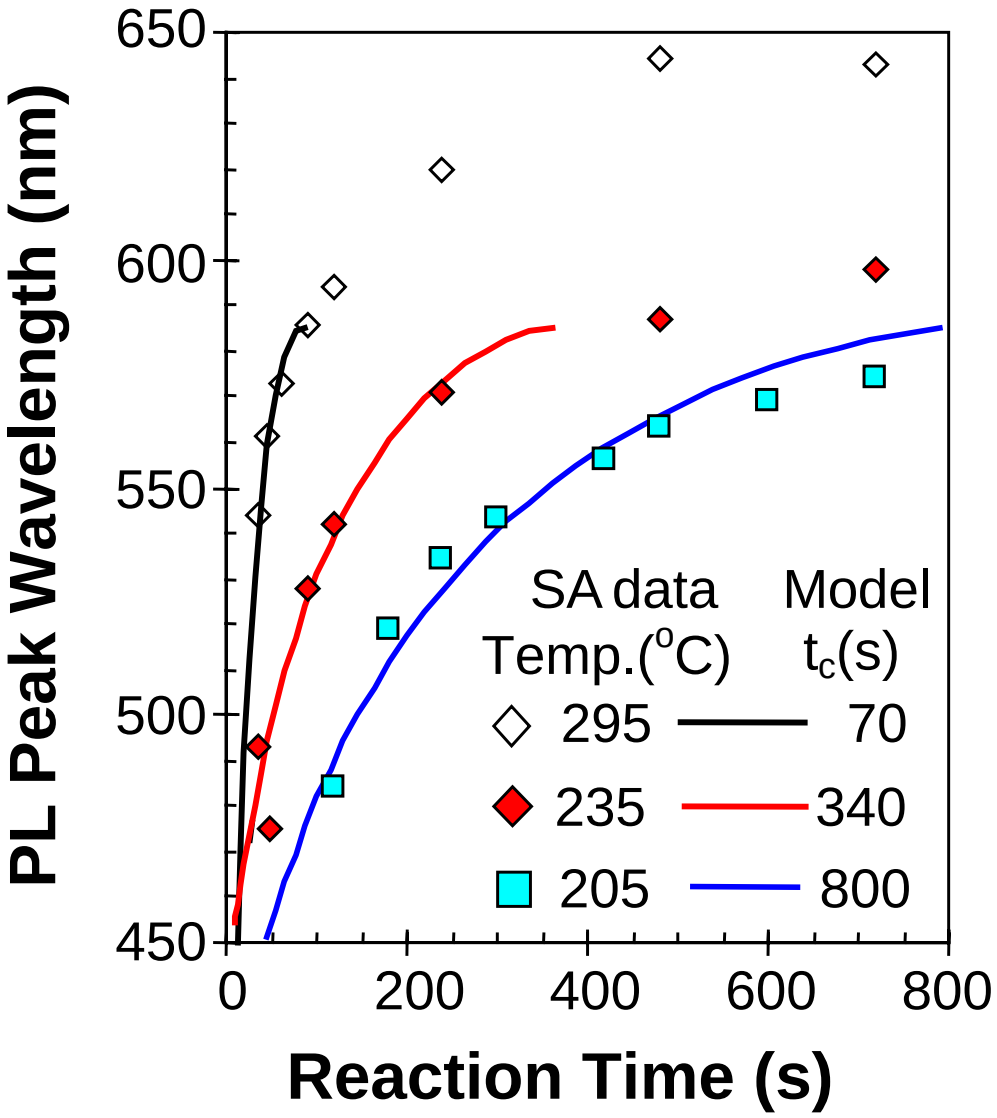

Figure 6-25. Fitting λ_{PL} versus reaction time to estimate reaction completion times, t_c.

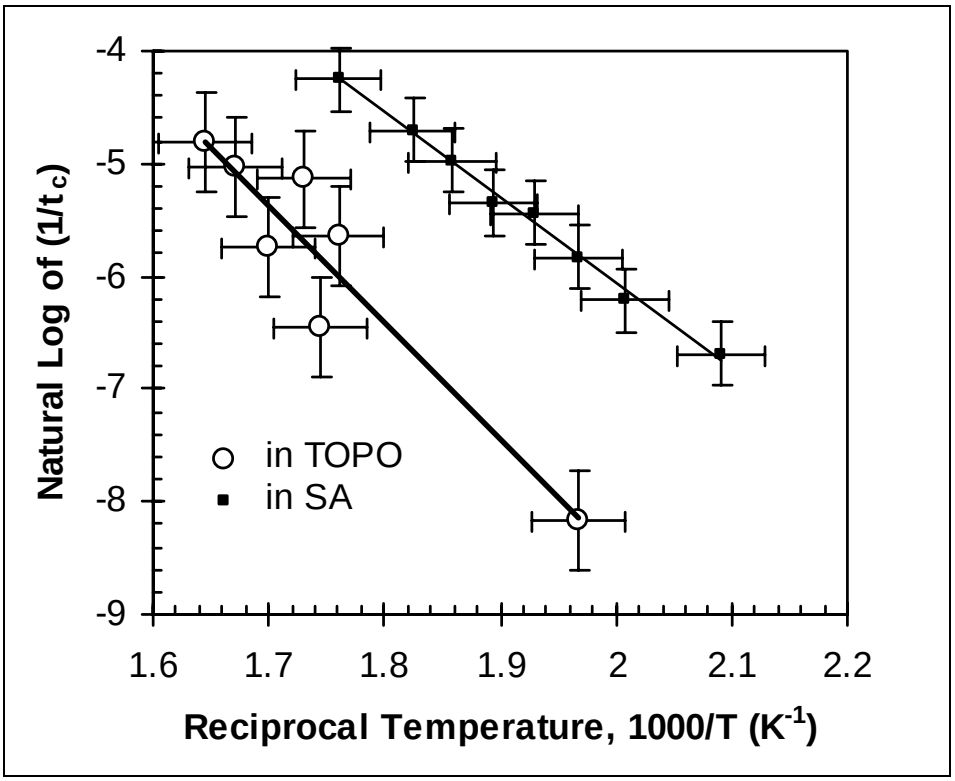

Figure 6-26. Arrhenius plot used to estimate *Q* from reaction completion times, t_c. This figure was reprinted with permission from Dickerson et al., Appl. Phys. Lett., **86** 076518 (2005). Copyright 2005 American Institute of Physics.

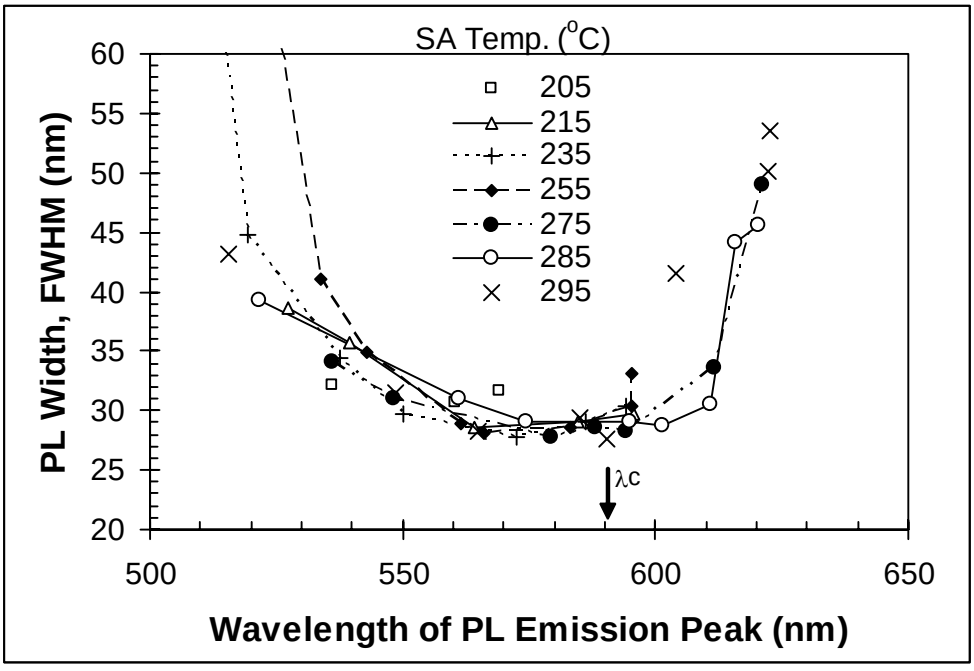

Figure 6-27. The narrowest FWHM occurs at λ_c independent of temperature in SA.

Effects of Se Concentration on Reaction Kinetics

Two different Cd:Se ratios were used for synthesis in TOPO in an oil bath at 285 °C . Over a period of 60 minutes, 25 samples were extracted and analyzed only using absorbance spectra. Figure 6-28 shows the absorbance spectra of the Cd-TOPO precursor solution and the Se-TOPO precursor solutions. The cadmium precursor showed broad band absorbance, with a small peak at 600 nm. Dilution of the cadmium precursor to 10% of the original concentration reduced the absorbance value at 650 nm to 10% of its original level. The selenium precursor was completely transparent over the optical wavelengths shown.

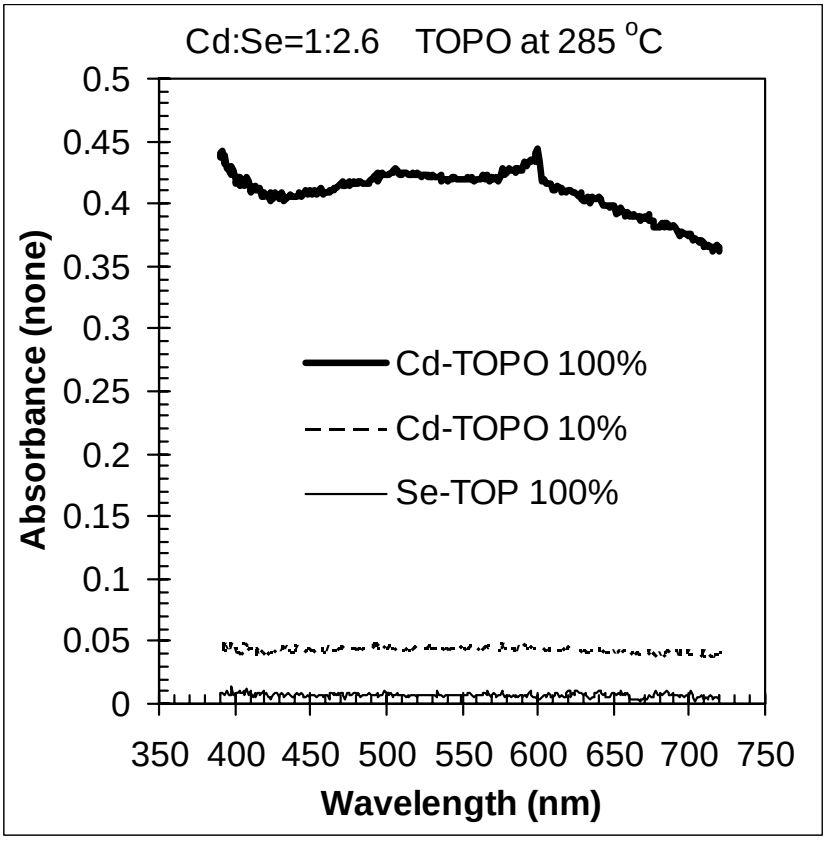

Figure 6-28. Precursor absorbance spectra. The Cd-TOPO-TDPA precursor has broad absorbance that is proportional to its concentration. The Se-TOP precursor is transparent over the visible part of the spectrum. Both precursors were for a Cd:Se ratio of 1:2.6.

For the Cd:Se ratio of 1:1.3, selected absorbance spectra observed soon after nucleation, at t_c, and much later in the reaction, are shown in Figure 6-29. Absorbance is a dimensionless optical property defined as $\log_{10}(100/Trans)$, where *Trans* is the percent transmission through the sample. In this work, the optical path length is always 1 cm. The background absorbance *B* at 650 nm gradually decreased with synthesis time, as cadmium precursors were consumed. The magnitude of the peak absorbance *A* gradually increased as the first absorbance peak λ_{abs} moved toward longer wavelengths with synthesis time. The difference A-B provided a way to track the concentration of quantum dots separate from the background, which tracked the Cd concentration.

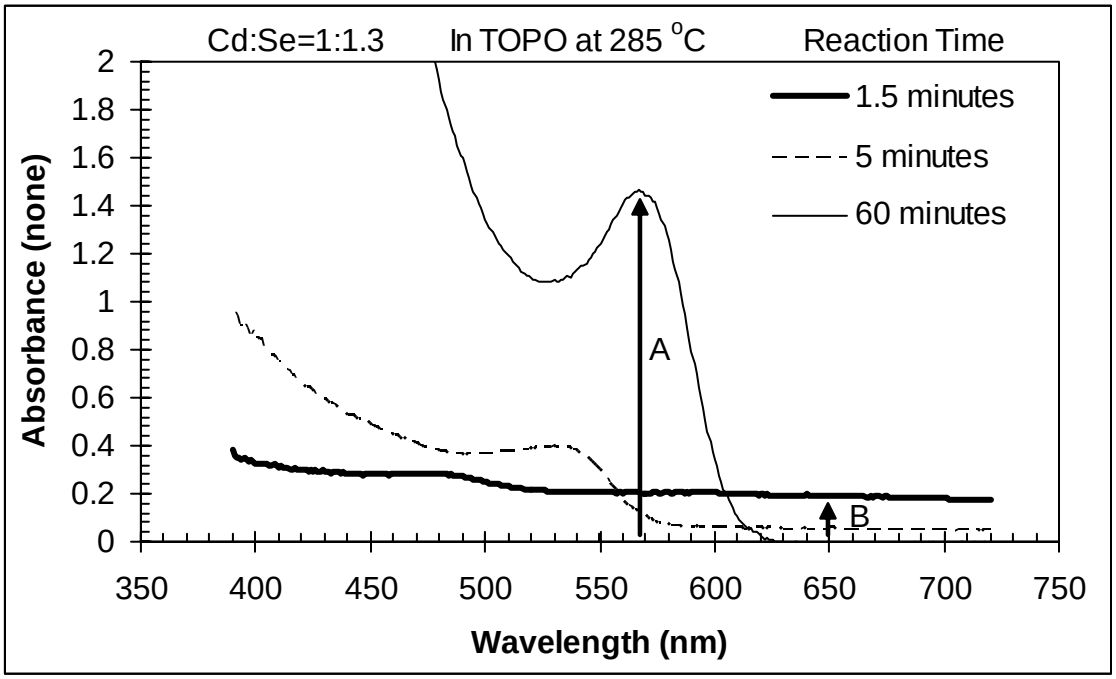

Figure 6-29. Selected absorbance spectra for Cd:Se = 1:1.3. The background level at 650 nm, B, the first absorbance peak wavelength, λ_{abs}, and its amplitude, *A*, all change with synthesis time in TOPO at 285 °C.

When the selenium concentration was doubled (Cd:Se = 1:2.6), the evolution of absorbance spectra was significantly different (Figure 6-30). The background level dropped more rapidly with synthesis time. In this series, the initial peak amplitude was higher and continued increasing until the completion time, beyond which the peak amplitude decreased.

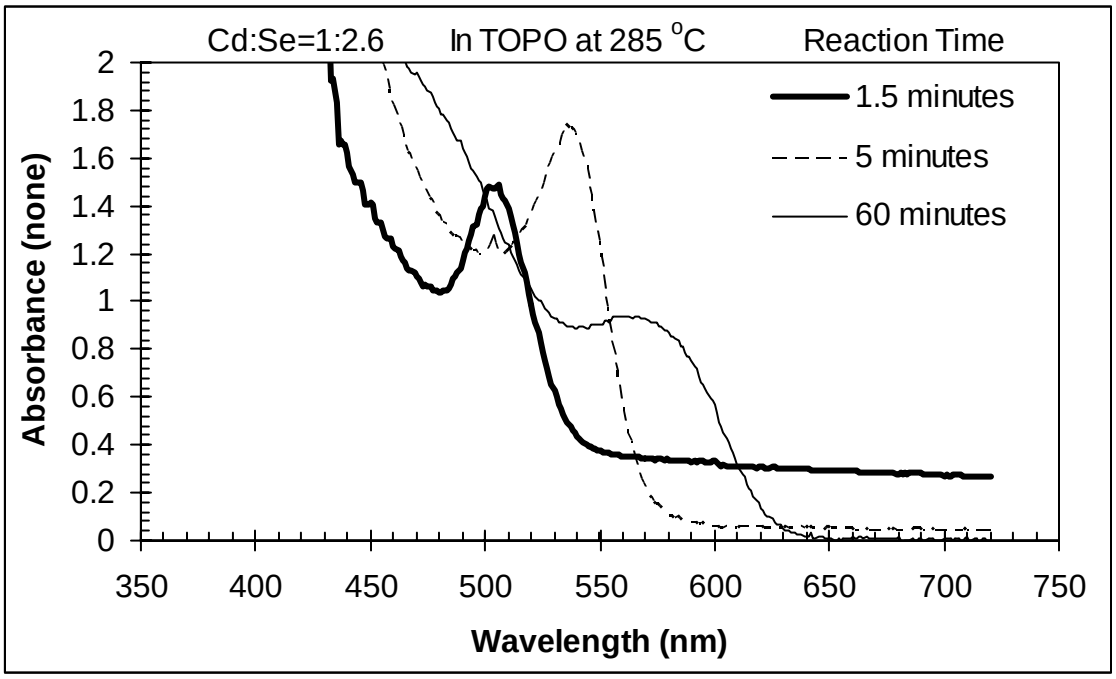

Figure 6-30.Variations in absorbance spectra at high Se levels (Cd:Se = 1:2.6). The first absorbance peak has a larger initial amplitude than normal, compared to Figure 6-29.

Regardless of the Cd:Se ratio, the wavelength of the first absorbance peak red-shifted with reaction time in nearly the same way, regardless of the selenium concentration (Figure 6-31). The early wavelength data was fit by diffusion models "a" (for Cd:Se = 1:1.3) and "b" (for Cd:Se = 1:2.6), with completion times of 360 s and 330 s, respectively. The model used Equation (6-3), with the input parameters shown, and resulted in estimates that about $2.4 \pm 0.1 \times 10^{18}$ nanocrystals formed, assuming a

reaction yield of 100%. Then from λ_{abs}, nanocrystal radius was estimated using the empirical conversion formula (6-4) discussed in Chapter 2. As seen in Figure 6-32, the quantum dot radius increased rapidly to about 1.4 nm at the completion time, followed by a more gradual size increase later in the reaction, as shown by Figure 6-32.

$$\lambda_{abs(t)} = \frac{hc}{E_g + X / R_{(t)}}, \text{ where } R_{(t)} = \left(\frac{(1 - \mathrm{f}_{(t)})\, C_o 3V_m}{4\pi N} \right)^{1/3} \text{ and } \mathrm{f}_{(t)} = \mathrm{f}_i \left(1 - \frac{\{t - t_i\}}{t_c} \right)^{3/2} \quad (6\text{-}3)$$

$$R_{(nm)} = \frac{X}{hc/\lambda_{abs} - E_g}, \text{ where } X = 0.82 \text{ eV nm} \quad (6\text{-}4)$$

Nanocrystal growth rate data points shown in Figure 6-33 were estimated from absorbance spectra parameters, using Equation (6-5), which was derived in Chapter 4. The diffusion model curve in Figure 6-33 predicted growth rates using Equation (6-6) based on the same input parameters used in Figure 6-31, except that an additional parameter, the diffusion velocity, *D/L*, was needed. Both selenium levels caused rapid growth rates immediately after nucleation, followed by gradually decreasing growth rates until the completion time, after which the growth rate was low and constant.

$$v = \frac{d\lambda_{PL}}{dt} \frac{R^4}{\lambda_{PL}^2} \frac{4\pi hc}{V_m X} \quad \text{from optical data} \quad (6\text{-}5)$$

$$v_{(t)} \approx 4\pi\, R_{(t)}^2 C_o \mathrm{f}_{(t)} (D / L) \quad \text{from the diffusion model} \quad (6\text{-}6)$$

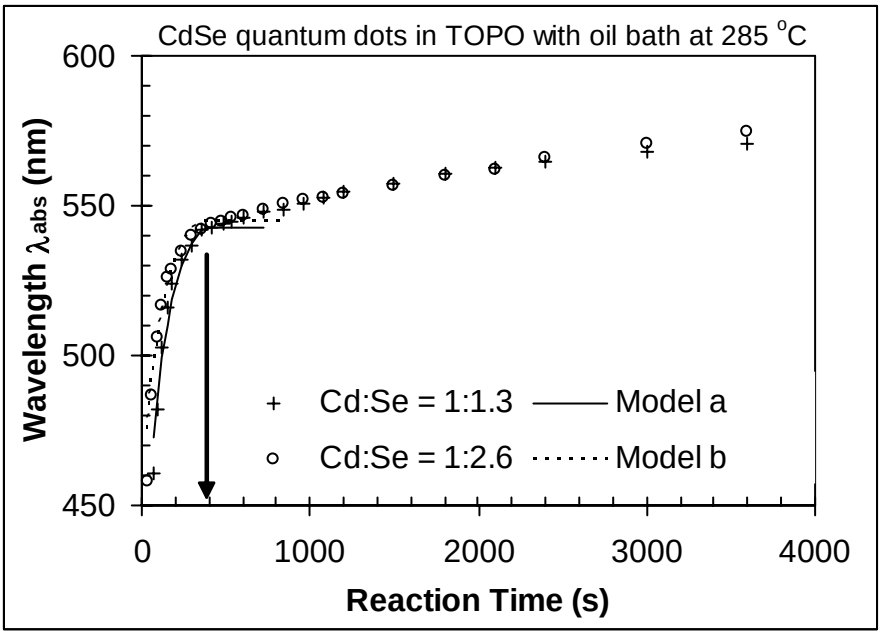

Model a	INPUT
D/L (cm/s)=	3.70E-07
λc(cm)=	5.43E-05
tc(s)=	360
fi=	0.9
ti (s)=	30
Neff(#)=	2.44E+18
Model b	INPUT
D/L (cm/s)=	3.70E-07
λc(cm)=	5.45E-05
tc(s)=	330
fi=	0.8
ti (s)=	20
Neff(#)=	2.30E+18

Figure 6-31. Evolution of absorbance peak wavelength. Data was fit by the diffusion model using the input parameters shown. The arrow marks a reaction completion at $t_i + t_c = 390$ s.

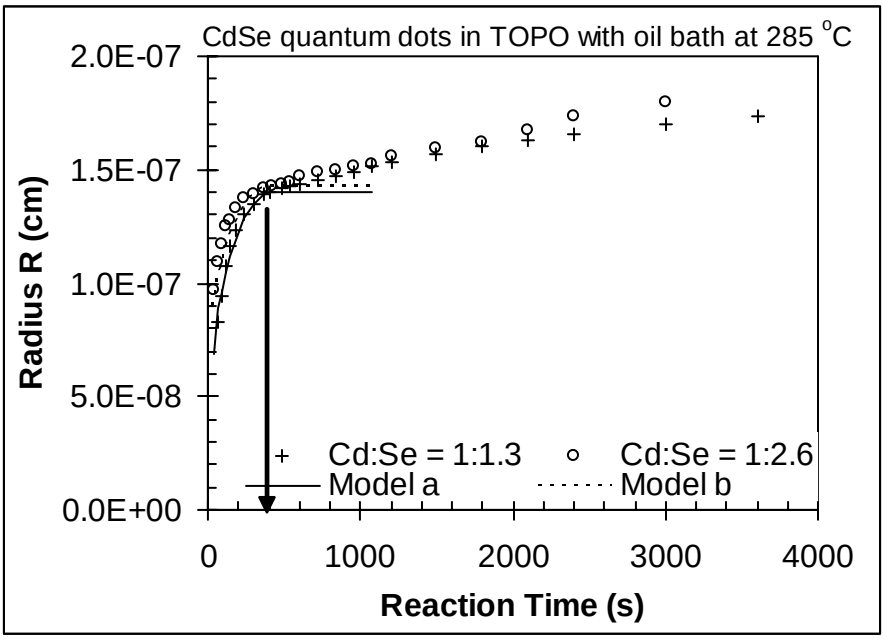

Model a	INPUT
D/L (cm/s)=	3.70E-07
λc(cm)=	5.43E-05
tc(s)=	360
fi=	0.9
ti (s)=	30
Neff(#)=	2.44E+18
Model b	INPUT
D/L (cm/s)=	3.70E-07
λc(cm)=	5.45E-05
tc(s)=	330
fi=	0.8
ti (s)=	20
Neff(#)=	2.30E+18

Figure 6-32. Growth of nanocrystal radius during synthesis in TOPO. The same model was used to fit wavelength evolution.

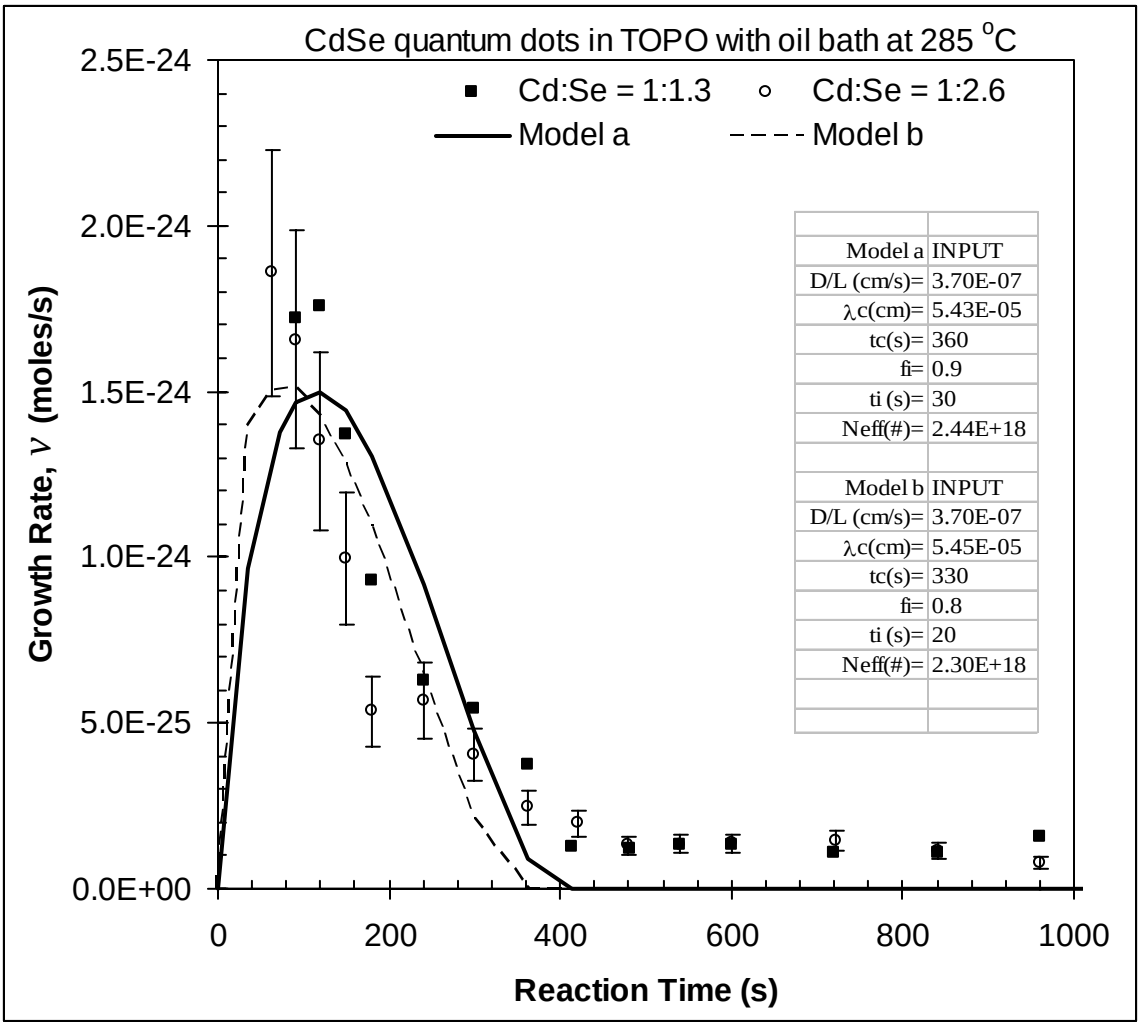

Figure 6-33. Growth rate versus reaction time.

The evolution of red-shift rates in Figure 6-34, followed the same trends seen in the growth rates. High initial red-shift rates decreased in magnitude until the completion time, then maintained a constant small positive red-shift rate. The rapid depletion of cadmium precursors during the reaction is shown in Figure 6-35, as determined by the background absorbance level at 650 nm for each sample, divided by the background level of the cadmium precursor solution. Although model "b" followed the depletion of precursors with high selenium levels, optical data suggested that Cd precursors were depleted over a longer time than estimated by model "a."

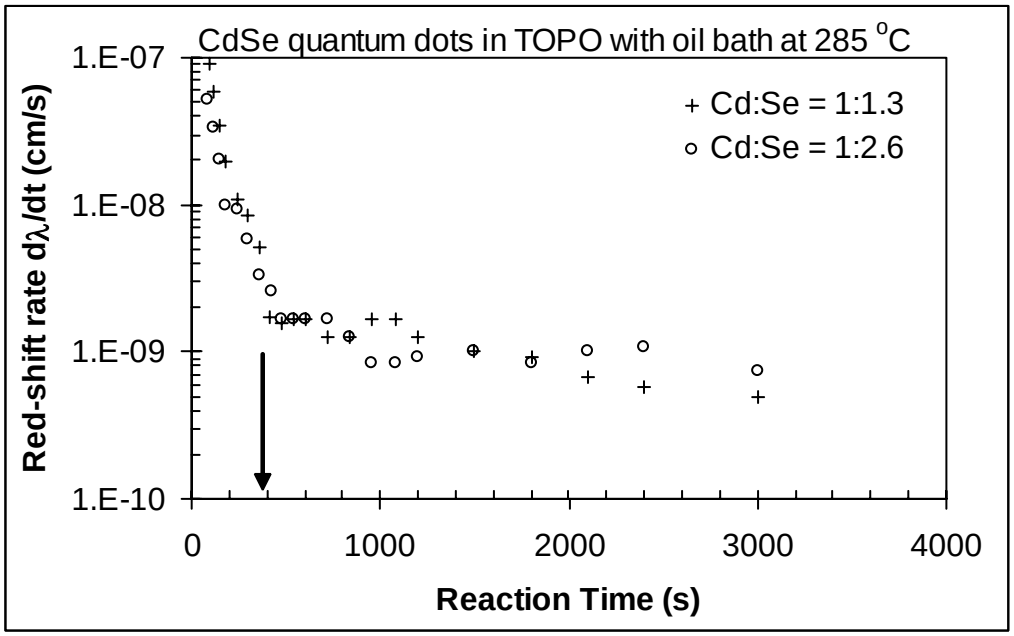

Figure 6-34. The red-shift rate, $d\lambda_{abs}/dt$, decreased to a low level when precursors were exhausted at t_c, indicated by an arrow. Compare to Figure 6-35.

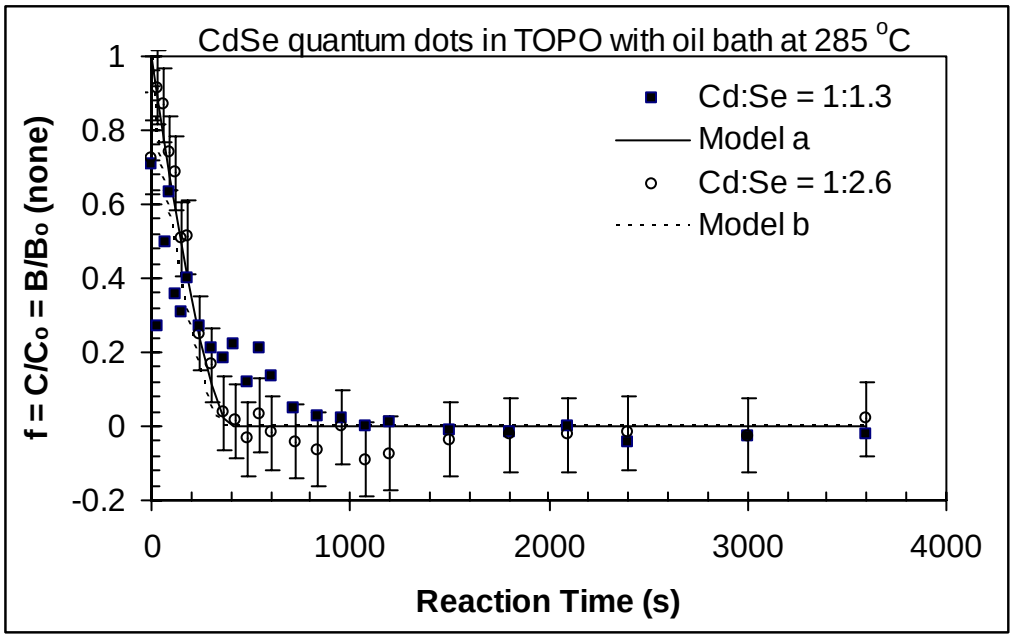

Figure 6-35. Rapid depletion of Cd precursors. C/C_o is the relative Cd concentration compared to the original concentration, C_o = 5.0 x 10^{-5} moles cm^{-3}. Data points were estimated from the absorbance background level, B, compared to the original level, B_o.

If the number of particles remains a constant, then the peak absorbance should increase with the total volume of suspended CdSe nanocrystals, according to Equation (6-7).[71] Here ε is the molar extinction coefficient (in $cm^{-1} M^{-1}$), $[M_{QD}]$ is the molar concentration of nanoparticles (in $mole^{-1}$ cm^{-3}), L is the optical path length of 1.00 cm, the coefficient α_ε is 1600 $x10^{24}$ cm^{-1} $mole^{-1}$ eV^{-1}, E_{abs} is the photon energy of the first absorbance peak (in eV), R is the average nanocrystal radius (in cm), N is the actual total number of nanocrystals in the reaction, N_A is Avogadro's number (in $mole^{-1}$), the total reaction volume V_{org} is 16.95 cm^3, and the dilution ratio of sample volume to toluene volume $V_{sample}/V_{toluene}$ was 0.5 mL / 8 mL for the quenched absorbance solutions.

$$A - B = \varepsilon[M_{QD}]L = \left(\alpha_\varepsilon E_{abs} 8R^3\right)\left[\frac{N}{N_A V_{org}}\frac{V_{sample}}{V_{toluene}}\right]L \qquad (6\text{-}7)$$

To test this idea, Figure 6-36 shows a plot of peak absorbance, A, versus R^3E_{abs}. For smaller quantum dots formed before t_c, the slope was steeper with a higher Se concentration, suggesting a higher initial nuclei concentration, N. Inspection of (6-8) shows that the slope of A versus $R^3 E_{abs}$ is expected to be proportional to N.

Figure 6-37 plots the global depletion of precursors $V_{org}*dC/dt$ versus the growth rate of individual nanocrystals, v, experimentally estimated from absorbance spectra features using Equation (6-5) shown earlier. Data clustered around the origin represent measurements of very low growth rates after t_c. If the particle count was constant, then the slope would equal the effective number of particles, N_{eff} , that would be required to account for the consumption of Cd. For Cd:Se = 1:2.6, $N_{eff} \sim 3 \pm 1 \times 10^{18}$. With lower Se levels, there was too much scatter in the data to estimate a value of N_{eff} , but the slope and effective particle count would clearly be lower.

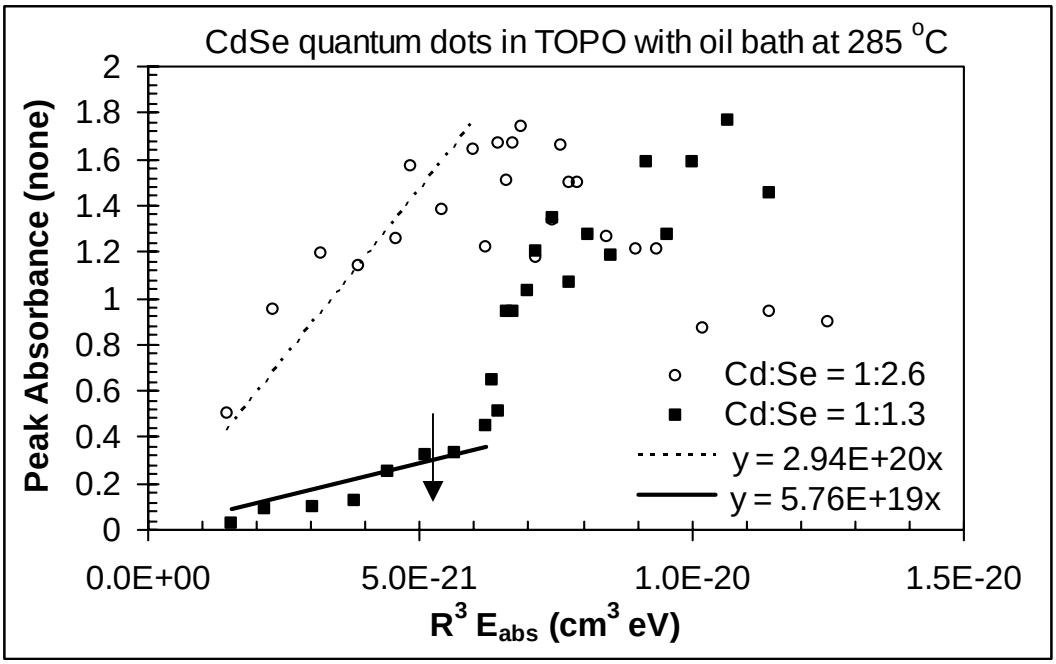

Figure 6-36. Peak absorbance versus ($R^3 * E_{abs}$). If N is constant, the slope is proportional to the number of CdSe nanocrystals, N. See text for Equation (6-7). The arrow marks a transition between sample properties at a reaction time of 390 s.

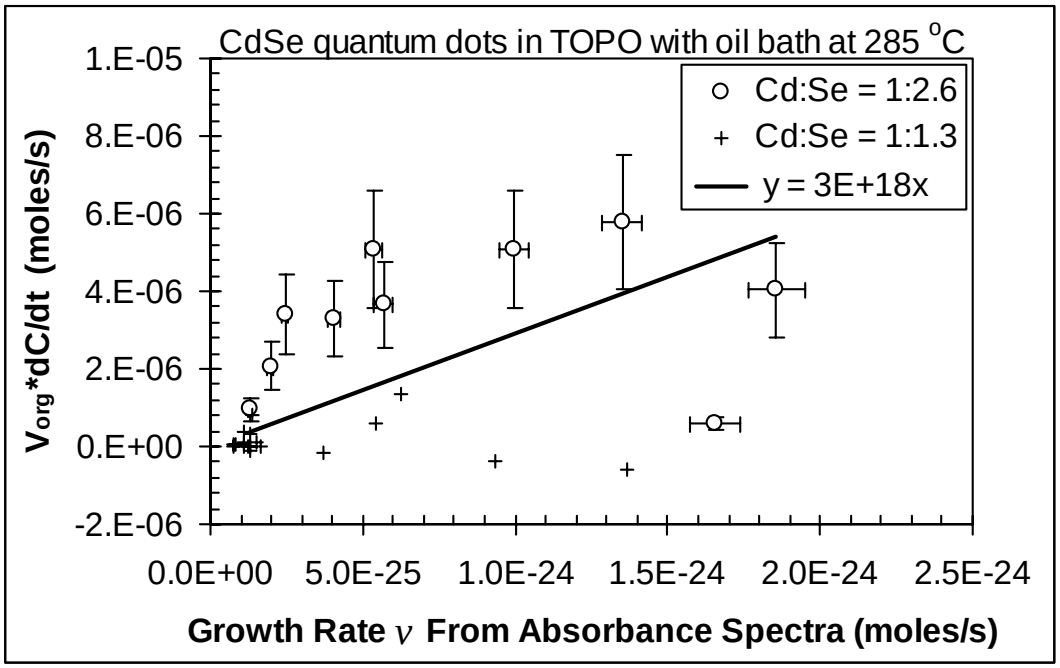

Figure 6-37. Reaction rate, $V_{org}*(dC/dt)$, versus nanocrystal growth rate, v. From absorbance spectra features, v was estimated using Equation (6-5). The slope of this plot is an estimate of the effective number of particles, $N_{eff} = 3 \pm 1 \times 10^{18}$.

To test whether the number of particles actually remained constant, N was estimated from the peak absorbance and the estimated nanocrystal radius using Equation (6-8), derived from (6-7). This optical data suggested that with normal Cd:Se ratios, the number of nuclei increased almost linearly during the first 1000 seconds and then stabilized (Figure 6-38). On the other hand, when the Se concentration was doubled, the number of nuclei initially was about 2×10^{18} (about 10 times higher than with a normal Cd:Se ratio of 1:1.3) and then decreased with reaction time almost exponentially. After 1000 seconds, the number of nuclei in both reactions was about 1×10^{18}.

$$N = \frac{(A-B)N_A V_{org}}{L\left(\alpha_\varepsilon E_{abs} 8R^3\right)}\left[\frac{V_{toluene}}{V_{sample}}\right] \qquad (6\text{-}8)$$

Other methods of estimating the number of nuclei shown in Figures 6-36 and 6-37 all agreed on one point: higher selenium levels seemed to facilitate the formation of more initial nuclei. Within experimental error, the estimates of N, based on individual quantum dot optical properties were comparable to the estimates for N_{eff}, based on the global depletion of Cd precursors.

The diffusion model (6-6) provided a conceptual basis for trying to estimate the diffusion rate, D/L. The model predicts that the growth rate, v, divided by $4\pi R^2 C$ should equal D/L. Therefore v, R, and C, were estimated from absorbance spectra (Figure 6-40a, b and c) using the methods displayed in Figures 6-33, 6-32, and 6-35, respectively. The points clustered around the origin represent slow growth rates after t_c. The slope for faster growing quantum dots (Figure 6-39) yielded an estimate for the diffusion velocity, $D/L \sim 2.5 \pm 0.5 \times 10^{-7}$ cm/s. The high degree of scatter in this data originates from uncertainties in the optical estimates of Cd precursor depletion during the reaction.

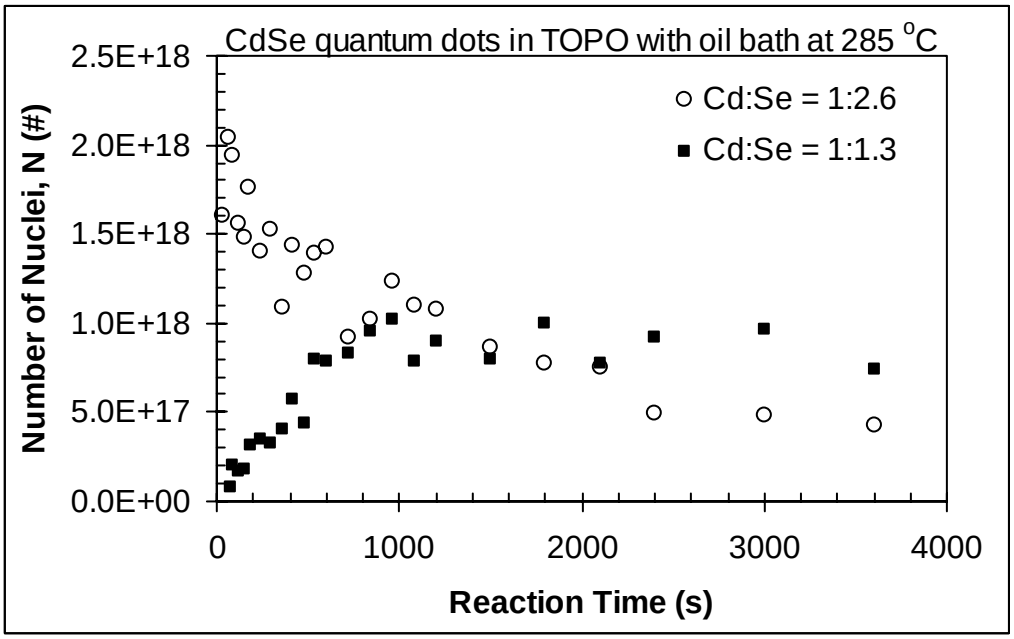

Figure 6-38. Changes in the number of nuclei during synthesis. Higher Se concentrations initially produced higher particle counts.

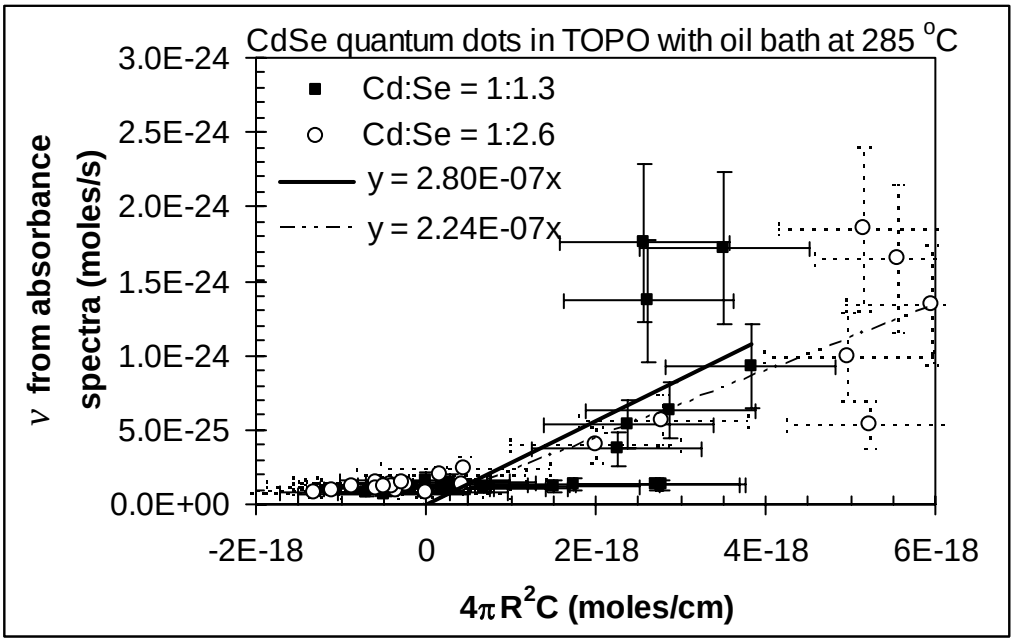

Figure 6-39. Graphical method of estimating *D/L*. In this plot of *v* versus Area*C, the slope is an estimate of *D/L* at 2.5 ± 0.5 x 10^{-7} cm/s.

Over-reliance on optical estimates of the Cd precursor concentration can create problems with modeling, as illustrated in Figure 6-40. In Figure 6-40 (a), the parameters t_c, f_i, and t_i were adjusted so that model "c" followed the cadmium precursor concentrations that were estimated from the background absorbance level for the reaction with normal selenium concentrations. Then in Figure 6-40 (b), only the completion wavelength was adjusted to improve the fit, while t_c, f_i, and t_i were fixed based on Figure 6-40 (a). However model "c" no longer follows experimental wavelength evolution. In Figure 6-40 (c), the previous parameters were maintained but the value of *D/L* was adjusted to improve the fit. However model "c" predicts a much slower decrease in the growth rate than is observed optically. Comparing Figure 6-40 (a) with 6-40 (c) shows that the cadmium precursor level apparently decreased over a longer time (~900 s), whereas the growth rate reached its minimum level within 420 s. This shows some of the limitations of estimating quantum dot growth solely from optical measurements.

To monitor another source of potential error, Figure 6-41 shows the temperature inside the reaction compared to the oil bath temperature during the reaction. Immediately after injection with a Se-TOP solution that was heated to 150 ^{o}C, the reaction temperature dropped significantly, but recovered in a few minutes, and stabilized to about 10 ^{o}C cooler than the oil bath.

A great deal of information about organometallic synthesis can be obtained using optical spectroscopy, thanks to the size-dependent optical properties of quantum dots. The implications of these results will be discussed in Chapter 7.

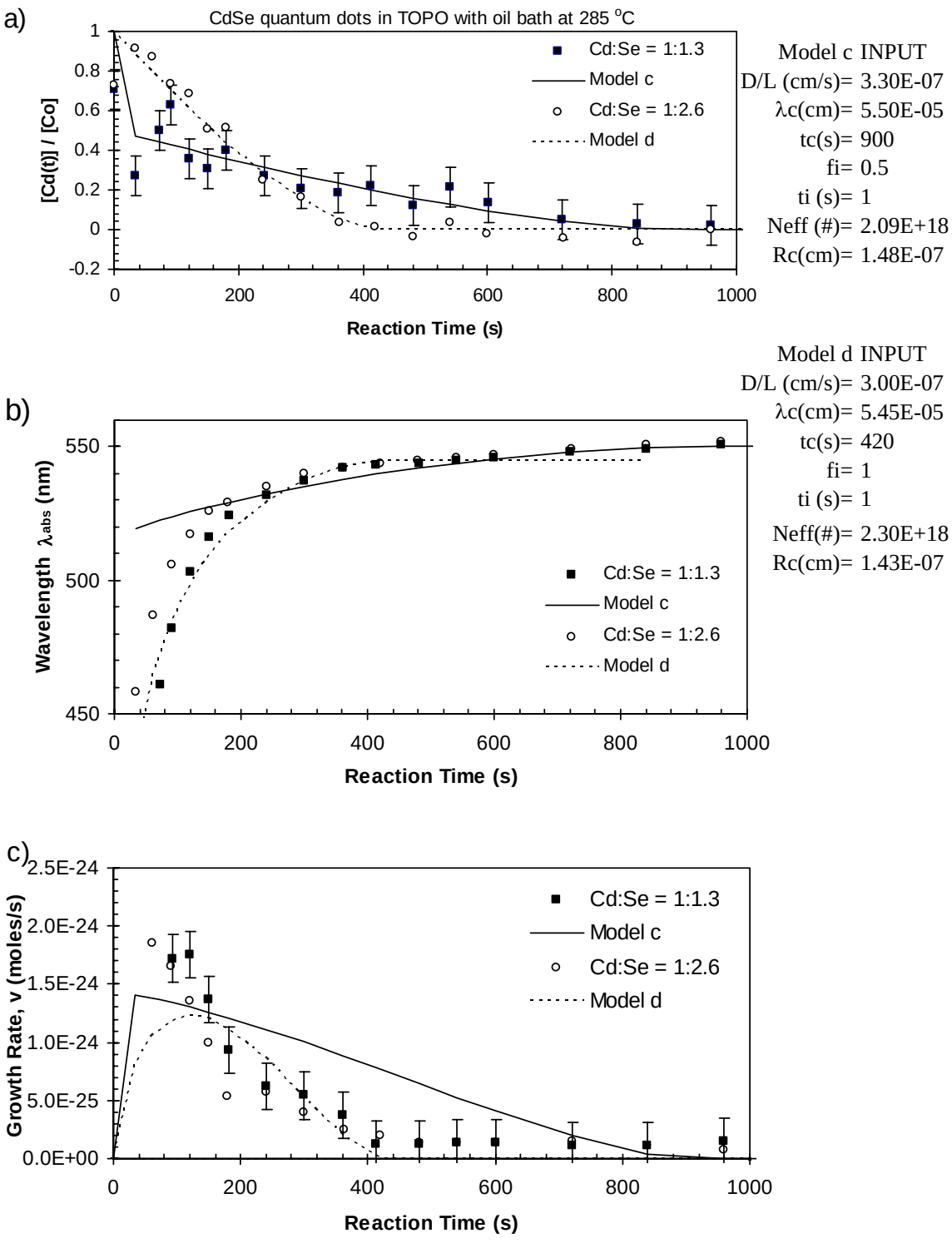

Figure 6-40. Fitting quantum dot growth based on optically monitored depletion of Cd precursors. The model was built in this order: a) f_i, t_i, and t_c were adjusted so that f would follow [Cd(t)]/[Co], b) λ_c was included to fit the evolution of λ_{abs}, c) then D/L was estimated to follow the growth rates, using all previous parameters.

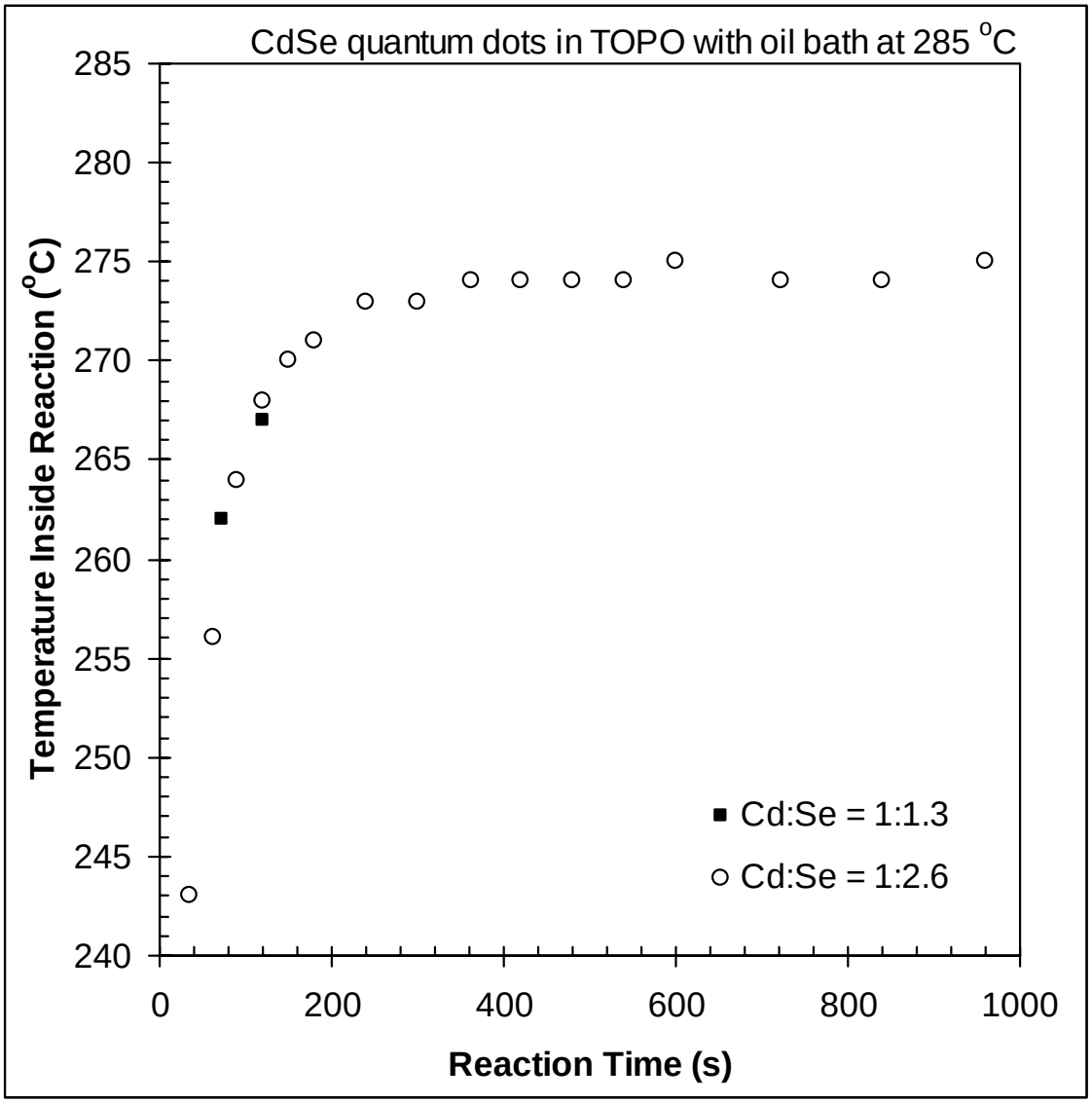

Figure 6-41. Variations in temperature early in growth. After injection of the Se-TOP precursor, the reaction solvent temperature was initially cooler but stabilized within 2 minutes to 10 °C below the oil bath temperature.